International Communications in Heat and Mass Transfer 179 (2026) 112107

Contents lists available at ScienceDirect

International Communications in Heat and Mass Transfer

journal homepage: www.elsevier.com/locate/ichmt

Finite-element and neural-network-assisted surrogate analysis of mixed convection heat transfer of nano-encapsulated phase change material suspensions in a lid-driven trapezoidal enclosure

Rawia Ahmed [a], Hanene Guesmi [a], Hany Alalfy [b], Jehan Habib [b], Jana Shafi [c], Khalil Hajlaoui [d], Mehdi Ghalambaz [e,*]

[a] Computer Science Department, Applied College, University of Ha'il, PO Box 2440, Ha'il City 55476, Saudi Arabia
[b] Management Information Systems Department, Applied College, University of Ha'il, PO Box 2440, Ha'il City 55476, Saudi Arabia
[c] Department of Computer Engineering and Information, College of Engineering in Wadi Alddawasir, Prince Sattam Bin Abdulaziz University, Saudi Arabia
[d] College of Engineering, Imam Mohammad Ibn Saud Islamic University (IMSIU), Riyadh, Saudi Arabia
[e] Department of Mathematical Sciences, Saveetha School of Engineering, SIMATS, Chennai, India

ARTICLE INFO

Dataset link: Dataset: Neural network-finite element study of heat transfer enhancement of nano-encapsulated phase change materials suspensions in a lid-driven trapezoid cavity (Original data)

Keywords:
Lid-driven cavity
Nano-encapsulated phase change materials suspension
Mixed convection
Dense neural network
Finite element method

ABSTRACT

This study investigates mixed convection heat transfer of nano-encapsulated phase change material (NEPCM) suspensions in a lid-driven trapezoidal enclosure with a W-shaped heated lower wall. The NEPCM suspension is modeled as a dilute Newtonian effective medium under local thermal equilibrium, and the latent heat effect of the encapsulated nonadecane core is incorporated through an effective heat-capacity formulation over a finite fusion-temperature interval. The dimensionless mass, momentum, and energy equations were solved using the finite element method for $0 \leq \phi \leq 0.05$, $0.1 \leq \theta_{fu} \leq 0.9$, $0.001 \leq \mathrm{Ri} \leq 1.0$, $30^{\circ} \leq \eta \leq 90^{\circ}$, and $0 \leq \chi \leq 0.5$. The results show that increasing the NEPCM concentration to 5% enhances the modified average Nusselt number by approximately 46% compared with the pure host fluid under the prescribed lid velocity. The optimum fusion temperature occurs near $\theta_{fu} \approx 0.2$, giving about 6% higher heat transfer at $\mathrm{Ri} = 1.0$, because the phase-change zone overlaps more effectively with the high-advection path generated by the moving cold lid. In addition to the FEM simulations, three surrogate models were evaluated: the recomputed linear correlation, a quadratic response surface model, and a compact dense artificial neural network. The independent test-set RMSE values were 0.5676, 0.0809, and 0.0685, respectively. Thus, the ANN is used as a fast nonlinear interpolation surrogate within the investigated FEM parameter space, not as a replacement for the FEM solver. The results provide design guidelines for NEPCM-based closed-cavity thermal management: the fusion temperature should be selected to match the dominant convective transport path, and the heat-transfer gain from NEPCM loading should be balanced against the associated viscosity penalty.

1. Introduction

The advent of nanotechnology has brought about a paradigm shift in several applications of heat transfer domain, particularly the convection processes. The heat transfer and radiation have found important applications in cooling of electronic components [1] and photovoltaic systems [2]. A significant advancement in this field involves the incorporation of nano-encapsulated phase change materials (NEPCMs) into heat transfer fluids, offering substantial potential for improving the thermal performance of energy systems [3,4].

Nano-encapsulated phase change materials (NEPCMs) represent an advanced class of thermal energy storage materials characterized by a phase change core encapsulated within a nanoscale protective shell. This unique configuration combines the high energy storage density of PCMs with the enhanced thermal and stability properties afforded by nanoscale encapsulation [4,5]. PCMs have long been recognized for their high latent heat storage capacity, they have the ability, during the process of phase transition, to store and release heat energy in large quantities, making them appropriate for thermal energy storage applications [6]. However, their practical use has been limited by several challenges, such as low thermal conductivity and phase segregation

* Corresponding author.
E-mail addresses: ri.ahmad@uoh.edu.sa (R. Ahmed), hs.gasmi@uoh.edu.sa (H. Guesmi), j.habib@uoh.edu.sa (J. Habib), j.jana@psau.edu.sa (J. Shafi), kmhajlaoui@imamu.edu.sa (K. Hajlaoui), ghalambaz.mehdi@gmail.com (M. Ghalambaz).

https://doi.org/10.1016/j.icheatmasstransfer.2026.112107

Nomenclature

Latin letters

Cp	specific heat capacity (J/kg K)
Cr	heat capacity ratio
Cr	heat capacity ratio function
Err	estimated computational error
f	non-dimensional fusion function
g	gravitational acceleration (m^2/s)
Gr	Grashof number
h	thermal convective coefficient (W/m^2 K)
H	enclosure height (m)
h_{sf}	enthalpy of phase change (J/kg)
k	thermal conductivity coefficient (W/m K)
L	enclosure width (m)
n	normal vector to surface (m)
N	non-dimensional normal vector to surface
Nc	number of thermal conductivity
Nm	mesh resolution parameter
Nu	average Nusselt number
Nu_a	modified average Nusselt number
Nul	Nusselt number, local
Nv	number of viscosity
p	Pressure field (Pa)
p_{CGI}	apparent order of grid convergence used in the GCI analysis
P	non-dimensional pressure field
Pr	Prandtl
Re	Reynolds
Ri	Richardson
Ste	Stefan number
T	field temperature (K)
Tc	temperature for cold surface (K)
T_{fu}	nanoparticles fusion temperature (K)
Th	hot wall temperature (K)
T_{Mr}	fusion temperature interval (K)
U	non-dimensional velocity in X-direction
u	x-direction velocity component (m/s)
U_t	lid driven velocity (m/s)
v	y-velocity component (m/s)
V	non-dimensional y-velocity component
x	horizontal Cartesian coordinate (m)
X	scaled x coordinate
y	vertical Cartesian coordinate (m)
Y	scaled y coordinate

Greek symbols

α	heat diffusivity (m^2/s)
β	volumetric thermal expansion coefficient (1/K)
δ	scaled fusion temperature bond
ζ	bottom wall shape parameter
η	enclosure side wall inclination angle (°)
θ	non-dimensional temperature field
ι	NEPCM core-shell weight ratio
λ	sensible heat capacity ratio
μ	dynamic viscosity (kg/m s)
ρ	density (kg/m^3)
ϕ	NEPCM particles concentration
χ	non-dimensional bottom wall shape factor
ψ	non-dimensional stream function

Subscript

b	suspensions bulk properties
co	NEPCM core
f	host liquid
p	NEPCM particle
sh	NEPCM shell

[7,8]. The encapsulation of PCMs at the nanoscale has been shown to effectively mitigate these issues, leading to enhanced thermal properties and stability [7,8]. NEPCM suspensions are selected in the present work because they combine three heat-transfer mechanisms in a single working medium. First, the encapsulated PCM core provides latent heat storage and release over a prescribed fusion-temperature range. Second, the nanoscale encapsulation improves dispersion and reduces leakage and phase segregation compared with bulk PCM systems. Third, the suspension can be treated as a flowing heat-transfer medium, allowing latent heat storage to interact directly with convective transport. These features make NEPCM suspensions attractive for compact thermal management systems where both heat spreading and transient thermal buffering are required. In the present geometry, the moving cold lid and W-shaped heated wall create an asymmetric convective pathway, so the location of the NEPCM phase-change zone becomes an additional design parameter rather than only a material property.

Besides, in another approach, some researchers attempt to improve the heat transfer of PCMs by adding nanoparticles to the host PCM [9,10], known as NePCM. This approach is different from the NEPCM technique [8,11], nanofluids [12,13], and regular hybrid nanofluids [14]. In the NEPCM suspensions, the PCM is encapsulated as nanoparticles while in NePCMs the nanoparticles are added to PCMs, while in the nanofluids, the nanoparticles do not undergo a phase change. This is while in NEPCM suspensions, the nanoparticles undergo a phase transition and absorb/release latent heat. The phase change of bulk PCMs has been addressed in several research studies such as [15,16]. Elevating the NEPCM particle volume fraction from 0% to 2% yields a 33% improvement in the average heat transfer coefficient. [17]. This improvement leverages the latent heat capacity of PCMs and the thermal conductivity of nanoparticles, illustrating the synergistic potential of NEPCM in thermal management. Research into NEPCM's role in thermal systems has uncovered its impact across a spectrum of configurations and conditions. Optimal thermal performance has been linked to specific NEPCM fusion temperatures, highlighting the importance of tailored material properties [17].

Investigations into free convection in enclosures filled with NEPCM show that heat transfer is affected by enclosure geometry, NEPCM concentration, fusion temperature, Stefan number, Rayleigh or Richardson number, wall heating arrangement, enclosure inclination, wall waviness, porous-layer thickness, and magnetic or radiative effects [18,19]. The design of composite enclosures utilizing NEPCM has shown that adjusting variables such as the volume fraction of NEPCMs and porous layer configurations can substantially improve heat transfer performance [20].

Further studies have expanded on these findings, demonstrating that the thermal and flow characteristics in systems filled with NEPCM can significantly influence the efficiency and effectiveness of thermal management strategies. These include the impact of inclination and waviness in trapezoidal cavities filled with NEPCM [19], and the nuanced effects of heating profiles in square enclosures [21]. Additionally, the mathematical modeling of unsteady convective flow in composite enclosures subject to rotation highlights the potential of NEPCM in enhancing heat transfer under rotational dynamics [22].

The study of convection processes involving NEPCM suspensions is of significant interest due to their potential applications in a multitude of domains, such as electronics cooling [23], energy storage [3], building heating and cooling systems [24] and the food industry [5]. In particular, mixed convection, which involves both forced and free convection, is a complex phenomenon that is influenced by a multitude of factors, including the geometry of the system, the properties of the fluid, and the boundary [25,26].

The cavity of trapezoidal shape is a useful geometry that is adopted in modeling convection processes due to its relevance to many practical applications, such as electronic devices and solar collectors [27,28]. The lid-driven flow in a trapezoid cavity introduces an additional level of complexity, as the moving lid induces a forced convection component to the flow, leading to a rich diverse array of flow patterns and heat transfer behaviors [29].

Literature on the mixed convection of NEPCM suspensions in a lid-driven cavity of trapezoidal geometry is spare, despite the importance of this subject. Most studies have focused on free convection heat transfer in simple geometries such as crescent-shaped [30], rectangular [31], prismatic [32], wavy wall [33,34], grooved [35], I shape [36], L shape [37], and a cavity containing fins [38], or heated and cooled cylinders [39].

External vibrations introduced into a porous enclosure with NEPCM suspensions have markedly enhanced heat transfer characteristics, as evidenced by vibrational Rayleigh numbers ranging from 1e6 to 1e7, which increased the Nusselt number in the fluid by more than 3.5 times [40]. Modifications to the interfacial heat transfer coefficient and enclosure porosity also led to substantial changes in the Nusselt number, highlighting the NEPCM suspensions' responsiveness to both dynamic external conditions and structural variations within the enclosure. Further research has broadened our comprehension of NEPCM's role in thermal management, especially regarding entropy generation and the effects of thermal radiation. The application of magnetic fields in latent heat thermal energy storage systems, for example, demonstrated that changes in viscosity, thermal conductivity, and magnetic numbers can drastically modify the system's thermal dynamics and efficiency [41]. In another instance, the specific arrangement and physical attributes of NEPCMs in a cavity with localized heating were found to crucially influence hydrothermal behavior, with certain capsule loading intervals optimizing heat transfer [42]. Additionally, employing sophisticated models like the power-law and Darcy-Brinkman-Forchheimer for NEPCM suspensions in a trapezoidal cavity emphasized how porosity and the behavior of non-Newtonian fluids can significantly enhance heat transfer and minimize entropy production [43].

There exists a limited number of research endeavors probing into the mixed convection of NEPCM suspensions in enclosures. Herouz et al. [44] addressed the mixed convection coupled with magnetohydrodynamics impacts within a double lid-driven hexagonal porous area filled with NEPCMs, where the cavity housed a heated square barrier. The team employed the Galerkin finite element technique to evaluate the influence of aspects like the alignment and velocity of the wall, magnetic field intensity, and permeability of the enclosure. The research inferred that wall motion direction plays a role in thermal dynamics and both NEPCM particle concentration and cavity's permeability are pivotal in dictating the thermal energy migration. Additionally, as the magnetic field's power grows, there's a decline in heat transfer. Sadr et al. [45], in another study, zeroed in on the thermal attributes of NEPCMs. They centered their analysis on a heated spinning cylinder encased within cold-walled chambers. This research scrutinized the roles of the Grashof number, Reynolds number, and fusion temperature. The outcomes hint at an ideal fusion temperature hovering around or slightly leaning toward 0.5. The research further illustrated that a drop in energy retention could boost the Nusselt number. They also found that at elevated Grashof numbers, upping the Reynolds number causes a dip in the heat transmission rate. Factoring in NEPCM might surge the Nusselt number by a margin exceeding 13%.

A few studies have utilized the neural networks and artificial intelligence techniques to study the physical problems. For example, Ismail et al. [46] investigated the heat transmission of ternary hybrid nanofluids flow in the space between a disk and a cone. The successfully applied a neural network with a regression value next to unity and estimated the heat transfer characteristics. Recent PCM and NEPCM studies also show increasing attention to coupled transport regulation and data-driven prediction. Huang et al. [47] reviewed thermal-fluid-magnetic coupling mechanisms in composite phase change systems and emphasized that coupled transport regulation is becoming important for advanced PCM thermal management. Li et al. [48] investigated vortex-mode evolution and heat transfer in metal foam/nanoparticle composite PCM under the combined action of centrifugal and magnetic fields. These studies demonstrate the broader importance of multi-physics regulation in PCM systems, but they focus on composite PCM or metal-foam/nanoparticle PCM systems rather than dilute NEPCM suspension in a closed lid-driven enclosure.

To more clearly establish the novelty of the present work, Table 1 compares the present configuration with representative NEPCM-based heat-transfer studies. The comparison is organized according to geometry, governing physics, methodology or main finding, and the specific difference from the present study. Previous studies have investigated NEPCM suspensions in rectangular, prismatic, wavy, grooved, finned, porous, magnetic, radiative, vibrational, and rotating-cylinder configurations. However, the simultaneous effects of lid-driven mixed convection, trapezoidal side-wall inclination, W-shaped heated wall geometry, NEPCM concentration, Richardson number, and fusion temperature have not been jointly examined for the present configuration.

As summarized in Table 1, the previous studies provide important insight into NEPCM heat-transfer enhancement through natural convection, porous media, radiation, magnetic fields, vibration, complex cavity shapes, fins, and rotating bodies. Nevertheless, these studies generally use either external control mechanisms, such as magnetic fields or vibration, or different geometries, such as rectangular, wavy, porous, grooved, hexagonal, or rotating-cylinder cavities. In contrast, the present study isolates the combined effect of passive W-wall geometry and lid-driven advection in a nonporous trapezoidal enclosure. This comparison clarifies that the novelty of the present work is not only the use of a new enclosure shape, but the coupled analysis of asymmetric lid-driven transport, W-wall heat-transfer-area modification, NEPCM latent heat storage, and surrogate-model comparison within the same FEM-generated database.

The study of mixed convection heat transfer in the context of NEPCMs suspensions represents a burgeoning field of interest. Prior research has largely concentrated on channel flows and the phenomena of free convection heat transfer. This present study aims to fill the existing gap in knowledge by investigating the mixed convection processes involving NEPCM suspensions within a lid-driven trapezoidal enclosure—an endeavor not previously explored. The effects of various factors on enhancing heat transfer, including the design intricacies of the cavity, the density of nanoparticles, the mixed convection parameter (referred to as the Richardson number), and the phase change temperature of the nanoparticles was addressed.

Based on the literature comparison, the knowledge gap addressed in this work is the lack of a combined analysis of NEPCM-assisted mixed convection in a lid-driven trapezoidal enclosure with a W-shaped heated wall. Existing studies have examined NEPCM suspensions in square, rectangular, wavy, porous, grooved, or magnetically controlled enclosures, but the simultaneous effects of lid-driven advection, trapezoidal inclination, W-wall shape factor, particle concentration, fusion temperature, and Richardson number have not been jointly resolved for this configuration. This combination is important because the moving cold lid creates an asymmetric circulation path, while the W-shaped heated wall modifies both the heat-transfer area and the local thermal-boundary-layer structure.

The novelty of the present work is therefore twofold. First, the FEM simulations clarify the physical mechanism by which the NEPCM phase-change region interacts with the asymmetric lid-driven flow. This explains why the optimum fusion temperature shifts toward $\theta_{\mathrm{fu}} \approx 0.2$,

Table 1
Literature comparison of NEPCM heat-transfer enhancement and machine-learning-assisted surrogate modeling studies with the present lid-driven W-wall trapezoidal enclosure. The comparison emphasizes geometry, governing physics, methodology/main findings, and the distinction from the present work.

Study	Geometry and physical model	Main method/focus	Difference from the present work
Golab et al. [31]	Rectangular cavity filled with NEPCM suspension	Natural convection and effect of NEPCM loading	No lid-driven mixed convection, no trapezoidal enclosure, no W-shaped heated wall, and no surrogate-model comparison
Ahmed and Raizah [32]	Inclined porous prismatic enclosure with NEPCM	Entropy generation and radiative flow	Focused on porous/radiative natural convection rather than lid-driven mixed convection in a nonporous W-wall trapezoidal enclosure
Hussain et al. [33] and Alazzam et al. [34]	Wavy or rectangular enclosures with NEPCM	Thermal radiation, bioconvection, magnetic-field effects	Considered external radiation/MHD effects, while the present work isolates geometry, lid motion, NEPCM concentration, and fusion temperature
Hussain et al. [35], Tayebi et al. [36], Sadeghi et al. [37], and Huu-Quan et al. [38]	Grooved, I-shaped, L-shaped, or finned enclosures	Effects of complex geometry or fins on NEPCM heat transfer	Did not examine the combined influence of trapezoidal side-wall angle, W-shaped heated wall, and lid-driven mixed convection
Cao et al. [39]	Energy-storage enclosure with heater/cooler arrangement	Heat transfer between localized hot and cold bodies	Different heating arrangement and no moving-lid-induced forced convection
Khedher et al. [40]	Porous enclosure filled with NEPCM under vibration	Vibrational enhancement of heat transfer	Heat transfer is enhanced by external vibration, whereas the present work uses a prescribed moving lid and passive geometry modification
Reddy and Sreedevi [41]	Magnetic NEPCM-based latent heat thermal storage system	Entropy generation and magnetic-field effects	Focused on MHD regulation; the present work does not use a magnetic field and instead studies lid-driven advection and geometric asymmetry
Wang et al. [42]	Cavity with localized heating and NEPCM suspension	Hydrothermal and entropy-generation analysis	Different heating configuration; no W-shaped heated wall and no ANN/RSM comparison
Kouki et al. [43]	Trapezoidal porous cavity with NEPCM suspension	Power-law and Darcy–Brinkman–Forchheimer models	Considered porous and non-Newtonian effects; the present study considers a dilute Newtonian suspension in a nonporous lid-driven W-wall enclosure
Herouz et al. [44]	Double lid-driven hexagonal porous cavity with NEPCM, obstacle, and magnetic field	Mixed convection with MHD and porous-medium effects	Different geometry and physics; the present work focuses on a single moving lid, trapezoidal enclosure, W-shaped heated wall, and fusion-temperature optimization
Sadr et al. [45]	Square cavity with rotating hot cylinder and NEPCM suspension	Mixed convection and effect of fusion temperature	Reported an optimum fusion temperature near 0.5, while the present work shows a shift toward $\theta_{fu} \approx 0.2$ due to asymmetric lid-driven transport
Galal et al. [49]	Wavy porous enclosure with nano-encapsulated PCM and thermal radiation	Neural modeling of NEPCM convection and heat-transfer response	Uses a porous/radiative wavy enclosure; does not examine lid-driven trapezoidal W-wall mixed convection or compare ANN with RSM and linear correlation
Tayebi et al. [50]	Oblique enclosure containing NEPCM-dielectric suspension	ANN prediction of electrohydrodynamic thermosolutal buoyancy-driven convection	Includes EHD and thermosolutal effects; different geometry and physics from

(continued on next page)

Table 1 (*continued*)

Study	Geometry and physical model	Main method/focus	Difference from the present work
	with active blocks		the present nonporous lid-driven W-wall enclosure
Ohid et al. [51]	Dielectric non-Newtonian fluid with active heat-transfer enhancement	Machine-learning approach for active heat-transfer amelioration	Does not involve NEPCM suspension in a lid-driven trapezoidal W-wall cavity
Alqurashi et al. [52]	MHD lid-driven curvilinear cavity containing NEPCM	Comparative machine-learning analysis of double-diffusive mixed convection	Includes MHD, double diffusion, and curvilinear geometry; different from the present passive W-wall trapezoidal enclosure
Alomari et al. [53]	Multi-port NEPCM cooling device	Thermodynamic analysis of mixed convection and MHD effects	Focuses on a multi-port cooling device and MHD regulation; not a closed trapezoidal W-wall lid-driven enclosure
Recent ANN-assisted NEPCM studies	Wavy porous, EHD, MHD, or curvilinear cavities with neural-network prediction	Machine-learning-based prediction of heat-transfer outputs	The present work compares ANN directly against a recomputed linear correlation and a quadratic RSM using the same group-aware test split, clarifying the added value of ANN relative to simpler baselines
Present study	Lid-driven trapezoidal enclosure with W-shaped heated wall filled with dilute NEPCM suspension	FEM, recomputed linear correlation, quadratic RSM, and compact ANN	Jointly examines lid-driven advection, trapezoidal angle, W-wall shape factor, NEPCM concentration, fusion temperature, and Richardson number; identifies the low-fusion-temperature optimum and validates the ANN against simpler surrogate models

rather than remaining near the commonly reported value of 0.5 for more symmetric natural-convection systems. Second, the FEM-generated database is used to construct and compare surrogate models of increasing complexity. The recomputed linear correlation provides a transparent first-order engineering estimate, the quadratic RSM provides an interpretable nonlinear baseline, and the compact ANN provides the lowest average interpolation error within the investigated parameter space. Thus, the study contributes both physical insight and a validated surrogate-model framework for rapid design-space exploration.

2. Physical model

Fig. 1 shows a schematic representation of a 2D trapezoidal chamber with a characteristic W-shaped lower boundary, containing a homogeneous mixture of water and NEPCM suspension. Such trapezoidal structures are prevalent in solar collector systems, glass manufacturing processes during annealing, and in aerospace for the cooling of electronic components. The NEPCM concentration ϕ, and chamber's upper cover remains cold, noted as T_c, and shifts rightward at a speed labeled U_t, while its bottom retains a higher temperature, noted as T_h. Both the height (H) and the length (L) of the chamber's base are identical, with H equal to L.

The nano-particles are featured in a zoomed-in view in Fig. 1, revealing a PCM encapsulation. The encapsulated particles undergo phase transitions between molten and crystalline states, regulating the storage and dissipation of thermal energy at a characteristic phase-change temperature T_{fu} (where $T_c < T_{fu} < T_h$). Additionally, Fig. 1 delineates the distinct morphological configurations exhibited by nanoparticles during thermal cycling, encompassing: (i) the baseline condition, (ii) the solidified low-temperature phase, and (iii) the liquefied high-energy state. The W-shaped base plays a critical role in supporting the chamber's lower wall, which not only fortifies the structural integrity but also expands the surface area, making this design particularly valuable for enhancing photovoltaic systems and solar collectors.

The trapezoidal angle, denoted by η, along with the parameter ζ that governs the bottom W wall, are integral to the chamber's geometry, as illustrated in Fig. 1. Despite changes in η, the dimensions H and L remain unchanged. Each nanoparticle comprises a polyurethane (PU) shell with a Nonadecane core—a phase change material. The NEPCM suspension demonstrates uniform dispersion characteristics, resulting in minimal velocity slip between the nanoscale capsules and base fluid. The submicron particle diameters produce thermally equilibrated systems with insignificant spatial temperature variations, validating their representation through the lumped-parameter approximation for phase-change particle analysis. Table 2 provides a systematic compilation of the thermophysical properties for the carrier fluid, phase-change core, and encapsulation matrix components. Noteworthy is the phase change

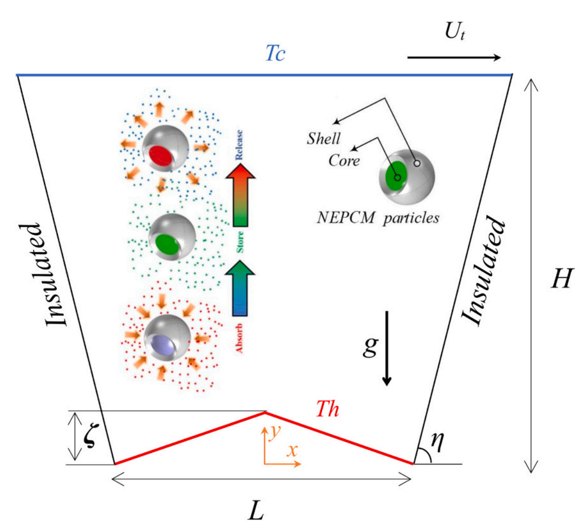

Fig. 1. A schematic of the computational domain and a representation of the physical model.

Table 2
The core (Nonadecane), the shell (PU), the host fluid, and the NEPCM particles [54].

	ρ (kg/m^3)	k (W/m.K)	μ (kg/m.s)	β (K^{-1})	Cp (KJ/kg.K)
Nonadecane	721	–	–	–	2037
PU	786	–	–	17.28×10^{-5}	1317.7
Host fluid	997.1	0.613	8.9×10^{-4}	21×10^{-5}	4179

temperature and its latent heat of fusion at 32 °C and 211 kJ/kg, respectively, as referenced from Barlak et al. [54].

2.1. The mathematical formulation

One presumes that the NEPCM suspension is consistent and exhibits characteristics of a Newtonian fluid. The particles are minuscule, and no temperature variations exist within them. The buoyancy forces are approximated by the Boussinesq approximation model. The nanoparticles and their host fluid maintain local thermal equilibrium. The homogeneous single-phase approximation is adopted because the present study is restricted to dilute NEPCM suspensions, $0 \le \phi \le 0.05$, and laminar flow conditions. Within this range, the NEPCM capsules are assumed to remain uniformly dispersed in the host liquid, and velocity slip between the capsules and base fluid is neglected. The suspension is therefore treated as a Newtonian effective medium. The local thermal equilibrium assumption implies that the host liquid, capsule shell, and PCM core have the same local temperature at the continuum scale. This assumption is commonly used for small encapsulated particles because the particle length scale is very small and not-significant temperature gradient can occur in such nano-meter size. The phase change process is not resolved inside each individual capsule; instead, its bulk effect is incorporated through the effective heat-capacity method over a finite fusion-temperature interval, T_{Mr}. Therefore, the present model should be interpreted as a continuum mixture model for dilute NEPCM suspensions rather than as a particle-resolved phase-change model. The modeling of the governing equations of mass momentum and energy conservation for hydrodynamic and thermal behaviors relies on the assumptions of a laminar, and incompressible suspension:

Mass conservation

$$\left(\frac{\partial u}{\partial x}+\frac{\partial v}{\partial y}\right)=0 \tag{1}$$

x- and y- momentum

$$\rho_b u\frac{\partial u}{\partial x}+\rho_b v\frac{\partial u}{\partial y}=-\frac{\partial p}{\partial x}+\mu_b\left(\frac{\partial^2 u}{\partial x^2}+\frac{\partial^2 u}{\partial y^2}\right) \tag{2}$$

$$\rho_b u\frac{\partial v}{\partial x}+\rho_b v\frac{\partial v}{\partial y}=-\frac{\partial p}{\partial y}+\mu_b\left(\frac{\partial^2 v}{\partial x^2}+\frac{\partial^2 v}{\partial y^2}\right)+g\rho_b\beta_b(T-Tc) \tag{3}$$

Energy equation

$$(\rho Cp)_b u\frac{\partial T}{\partial x}+(\rho C_p)_b v\frac{\partial T}{\partial y}=k_b\left(\frac{\partial^2 T}{\partial x^2}+\frac{\partial^2 T}{\partial y^2}\right) \tag{4}$$

The symbols in the above parameters have been introduced in the nomenclature. Any terms with the b subscript in the mentioned equations correspond to the bulk attributes of the suspension while the subscript f denotes the host fluid. Moreover, the corresponding boundary conditions can be written as:

$$\text{For the bottom wall}: u=v=0, T=T_h \tag{5}$$

$$\text{For the top wall}: u=U_t, v=0, T=T_c \tag{6}$$

$$\text{For side walls}: u=v=0, \frac{\partial T}{\partial n}=0 \tag{7}$$

where n is the surface normal vector.

2.2. Suspension properties

The estimation of the mixture's density is provided by [55]:

$$\rho_b=(1-\phi)\rho_f+\phi\rho_p \tag{8}$$

where the subscripts f and p symbolize the host liquid and NEPCM particles correspondingly. Additionally, the symbol ϕ stands for the NEPCM particles' concentration. Eq. (9) is utilized for calculating the NEPCM particles' density [55]:

$$\rho_p=(1+\iota)(\rho_{co}\rho_{sh})(\rho_{sh}+\iota\rho_{co})^{-1} \tag{9}$$

with ρ_{sh} and ρ_{co} denoting the densities of the particle's shell and core, respectively. The core-shell weight ratio is symbolized as ι, roughly valued at 0.447, see [54]. The heat capacity per unit of mass for the suspension is derived from the following equation [56,57]:

$$Cp_b=\rho_b^{-1}\left(\rho_f Cp_f(1-\phi)+\rho_p Cp_p\phi\right) \tag{10}$$

When there's no phase transition, the composite nanoparticle's effective heat capacity, referred to as Cp_p, is determined through (see [55]):

$$Cp_p=\frac{(\iota Cp_{sh}+Cp_{co})(\rho_{sh}\rho_{co})}{(\iota\rho_{co}+\rho_{sh})\rho_p} \tag{11}$$

One should observe that the heat capacity of the nanoparticle core represents an average between the fluid and solid phases' heat capacities. When the nanoparticle core experiences a phase transition, its specific heat capacity incorporates the latent heat of this change. This latent heat can be depicted through a sinusoidal profile, as indicated in references [55, 58]:

$$Cp_p=Cp_{co}+\left\{\frac{\pi}{2}\cdot\left(\frac{h_{sf}}{T_{Mr}}-Cp_{co}\right)\cdot\sin\left(\pi\frac{T-T_{fu}+T_{Mr}/2}{T_{Mr}}\right)\right\} \tag{12}$$

where the term T_{Mr} represents the temperature interval, which prevents temperature jump in the energy equation.The sum of latent and heat capacities of the particle core can be contributed to the heat equation using a phase change profile over a fusion range (T_{Mr}) [55,58]:

$$Cp_p=\left\{\frac{\pi}{2}\cdot\left(\frac{h_{sf}}{T_{Mr}}-Cp_{co}\right)\cdot\sin\left(\pi\frac{T-T_{fu}+T_{Mr}/2}{T_{Mr}}\right)\right\}\gamma+Cp_{co}$$
$$\gamma=\begin{cases}0 & T<[T_{fu}-T_{Mr}/2]\\ 1 & [T_{fu}-T_{Mr}/2]<T<[T_{Mr}/2+T_{fu}]\\ 0 & T>[T_{Mr}/2+T_{fu}]\end{cases} \tag{13}$$

The NEPCM-suspension's coefficient of thermal volume-expansion is given by Seyf et al. [58]:

$$\beta_b=(1-\phi)\beta_f+\phi\beta_p \tag{14}$$

The suspension's operative dynamic viscosity and thermal conductivity following (see [59,60])

$$\frac{\mu_b}{\mu_f}=(1+Nv\phi) \tag{15}$$

$$\frac{k_b}{k_f}=(1+Nc\phi) \tag{16}$$

Dynamic viscosity (Nv) and thermal conductivity (Nc) are empirical enhancement parameters for the dynamic viscosity and thermal conductivity of the NEPCM suspension. They are not universal constants; rather, they depend on capsule material, particle size, base fluid, preparation method, and operating temperature. In practice, *Nv* and *Nc* are impacted by a range of factors including nanoparticle characteristics (type and size), base fluid properties, overall operating temperature, and nanofluid preparation method [59–61]. Nevertheless, for specific produced nanofluids and operating conditions, these values can be treated as constants [59,60,62]. However, the formulation does not account for non-Newtonian rheology, particle aggregation, long-term suspension stability, or possible temperature dependence of *Nv* and *Nc*.

2.3. Dimensionless equations

To elucidate the general behavior of the mixture, the control equations and their corresponding boundary constraints were recast into a dimensionless form. This necessitated the introduction of specific dimensionless parameters:

$$X = \frac{x}{H},\quad Y = \frac{y}{H},\quad N = \frac{n}{H},\quad \chi = \frac{\zeta}{H},\quad P = \frac{p}{\rho U_t^2},\quad V = \frac{v}{U_t},\quad U = \frac{u}{U_t},\quad \theta = \frac{T - T_c}{\Delta T} \tag{17}$$

By incorporating the dimensionless variables into the fundamental equations, as detailed in Appendix A, a corresponding dimensionless equation set was derived:

$$\frac{\partial V}{\partial Y} + \frac{\partial U}{\partial X} = 0 \tag{18}$$

$$\left(\frac{\rho_b}{\rho_f}\right)\left(V\frac{\partial U}{\partial Y} + U\frac{\partial U}{\partial X}\right) = \frac{1}{\mathrm{Re}}\left(\frac{\mu_b}{\mu_f}\right)\left(\frac{\partial^2 U}{\partial Y^2} + \frac{\partial^2 U}{\partial X^2}\right) - \frac{\partial P}{\partial X} \tag{19}$$

$$\left(\frac{\rho_b}{\rho_f}\right)\left(V\frac{\partial V}{\partial Y} + U\frac{\partial V}{\partial X}\right) = \frac{1}{\mathrm{Re}}\left(\frac{\mu_b}{\mu_f}\right)\left(\frac{\partial^2 V}{\partial Y^2} + \frac{\partial^2 V}{\partial X^2}\right) - \frac{\partial P}{\partial Y} + \frac{(\rho\beta)_b}{(\rho\beta)_f}Ri\theta \tag{20}$$

The dimensionless parameters in the preceding equations, are: Grashof (*Gr*), Reynolds (*Re*), Prandtl (*Pr*), and Richardson (Ri) numbers, and are defined as:

$$\mathrm{Gr} = \frac{\rho_f{}^2 g\beta_f \Delta T H^3}{\mu_f{}^2},\ \mathrm{Pr} = \frac{\mu_f}{\rho_f \alpha_f},\ \mathrm{Re} = \frac{\rho_f U_t H}{\mu_f},\ \mathrm{Ri} = \frac{\mathrm{Gr}}{\mathrm{Re}^2} \tag{21}$$

where

$$\left(\frac{\beta_b}{\beta_f}\right) = (1-\phi) + \phi\frac{\beta_p}{\beta_f},\ \left(\frac{\rho_b}{\rho_f}\right) = (1-\phi) + \phi\frac{\rho_p}{\rho_f} \tag{22}$$

and $\alpha = k/(\rho Cp)$. Moreover, the expansion of NEPCM particles is presumed to be analogue to the host liquid, and thus $\beta_b/\beta_f \sim 1$ and $\rho_b/\rho_f \sim 0.74$.

$$Cr\left(U\frac{\partial \theta}{\partial X} + V\frac{\partial \theta}{\partial Y}\right) = \frac{1}{\mathrm{PrRe}}\left(\frac{k_b}{k_f}\right)\left(\frac{\partial^2 \theta}{\partial X^2} + \frac{\partial^2 \theta}{\partial Y^2}\right) \tag{23a}$$

Besides, the heat capacity ratio (*Cr*) is gained as a function of nanoparticles concentration, Stefan number (Ste), and the sensible heat capacity ratio (λ):

$$Cr = \frac{(\rho C_p)_b}{(\rho C_p)_f} = (1-\phi) + \phi\lambda + \phi\delta^{-1}Ste^{-1}f \tag{23b}$$

in which

$$\lambda = \frac{(C_{p,co} + \iota C_{p,sh})\rho_{co}\rho_{sh}}{(\rho C_p)_f(\rho_{sh} + \iota\rho_{co})},\ \delta = \frac{T_{Mr}}{\Delta T},\ \mathrm{Ste} = \frac{(\rho C_p)_f \Delta T(\rho_{sh} + \iota\rho_{co})}{h_{sf}\rho_{co}\rho_{sh}} \tag{24}$$

Furthermore, the dimensionless fusion function (*f*) is obtained as:

$$f = \frac{\pi}{2}\sin\left[\frac{\pi}{\delta}\left(\theta - \theta_{fu} + \delta/2\right)\right]\begin{cases} 0 & \theta < \left(-\dfrac{\delta}{2} + \theta_{fu}\right) \\ 1 & \left(-\dfrac{\delta}{2} + \theta_{fu}\right) < \theta < \left(\dfrac{\delta}{2} + \theta_{fu}\right) \\ 0 & \theta > \left(\dfrac{\delta}{2} + \theta_{fu}\right) \end{cases} \tag{25}$$

in which the dimensionless melting temperature (θ_{fu}) is introduced as:

$$\theta_{fu} = \frac{T_{fu} - Tc}{\Delta T} \tag{26}$$

Ultimately, the dimensionless boundary conditions are achieved following Appendix B:

$$\text{For the bottom wall}: \theta = 1,\quad U = V = 0 \tag{27}$$

$$\text{For the top wall}: \theta = 0,\quad U = 1, V = 0 \tag{28}$$

$$\text{For the side walls: } \frac{\partial \theta}{\partial N} = 0,\quad U = V = 0 \tag{29}$$

The local and average Nusselt number at the bottom wall which is used to characterize heat transfer can be introduced as:

$$Nu_l = -\left(\frac{k_b}{k_f}\right)\left(\frac{\partial \theta}{\partial N}\right)\bigg|_{Bottom\ wall} = -(1 + Nc\phi)\left(\frac{\partial \theta}{\partial N}\right)\bigg|_{Bottom\ wall} \tag{30}$$

$$Nu = \frac{1}{S}\int_0^S Nu_l dS \tag{31}$$

and the modified average Nusselt number $\mathrm{Nu_a}$ is computed as:

$$Nu_a = \left(\frac{S}{L}\right)Nu \tag{32}$$

The term S/L includes the impact of the geometrical increase of the length of the bottom wall due to the W shape of the surface. A W shape surface can provide a larger surface of heat transfer. An augmentation in the χ parameter can extend the wall length (S), leading to a larger area for heat transfer. Therefore, to fully grasp the effect of χ on heat transfer rates, they utilized the adjusted average Nusselt number. For a regular definition of the local Nusselt number as $Nu_l = hH/k_f$, H and k_f are fixed and h is the heat transfer coefficient, which can be easily evaluated when Nu_l is known.

Besides, the following partial differential equation and corresponding boundary conditions were introduced to compute the streamlines using fluid velocities for the sake of visualizing the representation of free convection flows:

$$\left\{\frac{\partial^2 \Psi}{\partial Y^2} + \frac{\partial^2 \Psi}{\partial X^2}\right\} = \left[-\frac{\partial V}{\partial X} + \frac{\partial U}{\partial Y}\right] \tag{33}$$

where $\Psi = 0$ on all surfaces [63,64].

3. Numerical method and model verification

3.1. Finite element numerical method

The finite element method (FEM) was used to solve the governing equations numerically, addressing both boundary and initial conditions. This technique was particularly adept at managing the nonlinear challenges posed by phase transitions, as discussed in studies by [65,66]. Employing a variational approach to the differential equations and using second-order approximations for discretizing momentum and the heat equations, a system of algebraic residual equations was created using Gauss quadrature integration at the elemental level. The coupled system was then iteratively solved using the Newton-Raphson method, referenced in Kelley [67] and Deuflhard [68], with a damping factor of 0.8 to facilitate convergence. The computational process was optimized by employing the PARDISO parallel solver, as described in [69,70], allowing for efficient distributed processing. The precision of the solutions was ensured by setting a convergence criterion of less than 1E-4.

3.2. Mesh study

A study was conducted to evaluate the impact of grid resolution on the accuracy of computational results. This examination was based on a test case characterized by a series of parameters: Richardson number (Ri) at 1.0, Reynolds number (*Re*) at 100, Stefan number (Ste) at 0.3, dimensionless fusion temperature (θ_{fu}) at 0.2, Prandtl number (*Pr*) at 6.2, dimensionless conductivity (λ) at 0.33, dimensionless thickness (δ) at 0.05, number of dynamic viscosity (*Nv*) at 12.5, Number of conductivity (Nc) at 23.8, angle (η) at 60°, dimensionless amplitude (χ) at 0.3. The computational domain was segmented using a structured mesh, where the granularity of the mesh was controlled by the parameter *Nm*.

The results, encompassing both the average and local Nusselt numbers, are summarized in Table 3 and graphically represented along the heated boundary in Fig. 2. Table 3 reveals a progressive rise in computational requirements with increasing mesh refinement (*Nm*). This pattern is predictable since the number of quadrilateral (Quads) and edge elements increases alongside the rise in mesh resolution. Compared to a mesh with $Nm = 6$, a mesh with $Nm = 4$ yields a mere 0.1% discrepancy.

To provide a more rigorous mesh-independence assessment, the grid convergence index (GCI) method was also applied using the three finest meshes, Nm = 4, 5, 6. Since the number of quadrilateral elements scales approximately with Nm^2. The corresponding modified average Nusselt numbers were 14.407, 14.401, and 14.397 for Nm = 4, 5, and 6, respectively. The convergence was monotonic. Using these three grids, the apparent order of convergence was approximately $p_{CGI} = 1.0$. The fine-grid GCI for $Nm = 6$ was approximately 0.174%, while the GCI estimate associated with the selected $Nm = 4$ mesh was approximately 0.21%. In addition, the direct relative difference between $Nm = 4$ and $Nm = 6$ was only 0.07%. Therefore, $Nm = 4$ was selected for the parametric simulations because it provides grid-independent Nu_a values while substantially reducing computational cost compared with the finest mesh. Therefore, they selected the $Nm = 4$ mesh for subsequent simulations. Fig. 3 shows a view of the adopted mesh.

3.3. Model verification

The study's outcomes were cross-referenced with two other academic papers to validate the precision of the simulations. Initially, the average Nu determined in this investigation was set side by side with the results from Matin and Pop [71], who investigated the free convection heat transfer of Cu-Water nanofluids within an annular space. Table 4 lists the average *Nu* values from both this study and Matin and Pop [71], evaluated across varying nanoparticle volume concentrations. The present results show good agreement with the benchmark data of Matin and Pop [71].

To further corroborate the results, the heat transfer metrics from Turan et al. [72], researchers that probed into free convection heat

Table 3
Mesh specification and computed modified average Nusselt number (Nu_a) for various mesh resolutions.

Nm	Quads	Nu_a	*%Err
2	9191	14.434	0.3
3	20,250	14.418	0.1
4	36,000	14.407	0.1
5	56,250	14.401	0.0
6	81,000	14.397	–

* $\%Err = 100 \times (Nu\text{-}Nu_{@Nm=6})/Nu_{@Nm=6}$.

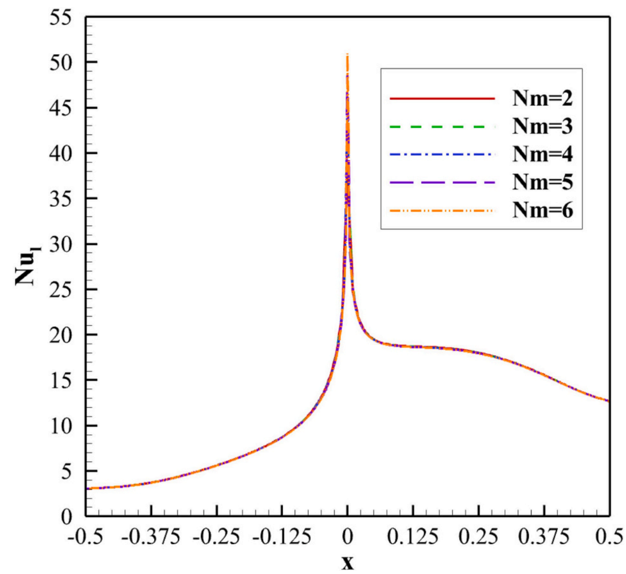

Fig. 2. Local Nusselt number for studied mesh sizes.

transfer in a cavity, were considered. In their study, they subjected the left and right vertical boundaries to contrasting temperature extremes, leaving the others devoid of any heat flow. Fig. 4 compares between the present study's findings and Turan et al. [72] results. When viewing Fig. 4, one can determine a good agreement between the data from this research and Turan et al. [72].

Lastly, Table 5 compares of the anticipated average Nusselt number in a cavity with heat applied at the top, cooling at the base, and insulation on the flanking sides. The results show that current simulation results and literature studies agree well.

In Fig. 5, there is a collocation of the isotherms and streamlines from this research with those detailed by Moallemi and Jang [73] and Roy et al. [64]. This is for an enclosure driven by the top lid, where heating occurs from the bottom, cooling from the top, and the side walls are insulated.

The remaining differences are small and can be attributed to differences in numerical discretization, mesh distribution, convergence tolerance, benchmark data extraction, and the treatment of boundary conditions near cavity corners. For example, in Table 5 at $Re = 1000$ and $Ri = 10^{-4}$, the present result differs from Roy et al. [64] by approximately 1.03%, from Waheed [74] by approximately 1.66%, and from Iwatsu et al. [75] by approximately 0.74%. These deviations are within the range typically expected for independent numerical implementations of mixed-convection benchmark problems. However, no experimental benchmark is available for the exact present configuration, namely a lid-driven trapezoidal enclosure with a W-shaped heated wall filled with NEPCM suspension. Thus, the results should be interpreted as numerically validated parametric trends within the adopted mixture-model assumptions.

4. Results and discussions

In this section, the impact of concentration of nanoparticles (NEPCMs) $0<\phi<0.05$, enclosure geometrical parameter $0 < \chi < 0.5$, Richardson number $0.001 < Ri < 1.0$, trapezoidal angle $30° < \eta < 90°$, and nanoparticles' fusion temperature $0.1 < \theta_{fu} < 0.9$ on the heat transfer rate has been investigated. The other parameters were considered fixed. The following values for parameters were adopted as a reference ϕ=0.05, Ri = 1.0, Ste. = 0.3, $\chi = 0.3$, $Re = 100$, $\theta_{fu} = 0.2$, $Pr = 6.2$, $\eta = 60°$, $\lambda = 0.33$, $Nc = 23.8$, $\delta = 0.05$, and $Nv = 12.5$. The range of these values are in agreement with the previous studies [64,74,76].

Fig. 6 depicts the effect of the trapezoidal angle (η) and geometrical

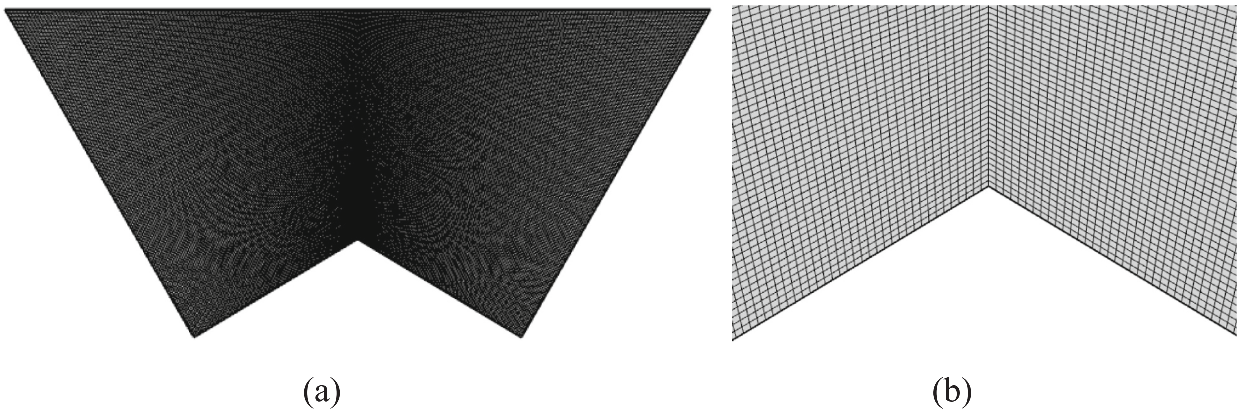

Fig. 3. Mesh size with $Nm = 4$: (a) A general view of the mesh, (b) A zoomed view of the mesh next to the W-wall.

Table 4
Comparison of mean Nusselt numbers between recent study and published literature.

ϕ	Matin and Pop [71]	Current study	Difference
0.03	6.02	6.09	−1.16%
0.02	5.89	5.87	0.34%
0.01	5.66	5.61	0.88%

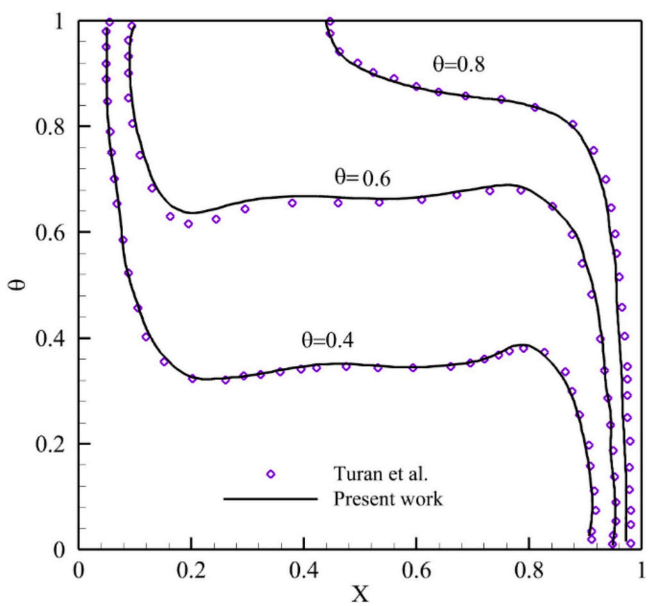

Fig. 4. Isotherm distributions simulated in the present research and those of Turan et al. [72]. θ: Ψ:

Table 5
The mean Nusselt number when considering a scenario of combined convection within a square enclosure filled with air (Prandtl number at 0.71), having a heated upper boundary, a cooled lower boundary, and side boundaries that do not transfer heat (adiabatic) with the Grashof number set at 100.

Re	Ri	Present study	Roy et al. [64]	Waheed [74]	Iwatsu et al. [75]
1	100	1.0001	0.998	1.00033	–
100	0.01	2.0340	1.967	2.03116	1.94
400	6.25×10^{-4}	4.0355	4.004	4.02462	3.84
500	4×10^{-4}	4.5272	4.509	4.52671	–
1000	1×10^{-4}	6.3767	6.443	6.48423	6.33

parameter of the W-wall (χ) on the modified average Nusselt number (Nu_a). As seen, the increase of χ raises Nu_a. This is because a rise of χ shifts the heated wall toward the cold top wall. Moreover, the increase in geometrical parameters impacts the mixed convection flows in a way that the fluid velocity next to the W wall increases. Fig. 7 exhibits the local Nusselt number for various trapezoidal degrees (η). As seen, an increase of η reduces Nu_l next to the side walls ($X = \pm 0.5$), but it has a minimal impact on the local Nusselt number in the middle ($X = 0$). This is evident in Figs. 8 for streamlines, isotherms, and heat capacity ratios for two cases $\eta = 60^\circ$ and $\eta = 75^\circ$. A small trapezoidal angle ($\eta = 60^\circ$) provides better room for flow circulation next to the bottom wall corners, which contributes to improving local heat transfer at $X = \pm 0.5$. This local improvement of heat transfer was observed in Fig. 7. Moreover, an increase of trapezoidal angle shifts the phase change region toward the top which consequently reduced the contribution of phase change heat transfer. The local Nusselt number profile experiences a significant escalation attributable to the bottom wall's contour. This wall design culminates in a pronounced apex at $X = 0$, where the heated surface encounters the circulating suspension directly. At this juncture, temperature gradients become particularly steep. Consequently, the local Nusselt number reaches its zenith at $X = 0$, maintaining elevated levels in adjacent areas as the central section benefits from continuous exposure to a fresh influx of cooler suspension. Additionally, the local Nusselt number on the left side ($X > 0$) consistently surpasses that on the right, a phenomenon influenced by the lid's motion, which propels the suspension in a clockwise direction, enhancing thermal exchange efficiency.

Fig. 9 vividly illustrates the profound impact of the Richardson number and the fusion temperature of nanoparticles on Nu_a. In a similar vein, Fig. 10 provides a detailed analysis of the local Nusselt number under a variety of nanoparticle fusion temperatures. These illustrative graphs confirm that the heat transfer rate undergoes a significant upturn with the elevation of the Richardson number. With a fixed Reynolds number ($Re = 100$), this rise in the Richardson number implies a corresponding growth in the Grashof number. This dynamic subsequently amplifies the potency of natural convection effects, enhancing the overall heat transfer process.

The effect of the fusion temperature (θ_{fu}) is another critical parameter. As θ_{fu} escalates, the phase change interface (visibly captured in Fig. 11 via Cr contours) gravitates toward the heated bottom wall. Interestingly, situating a phase change interface proximate to the lid-driven wall can foster a dispersed effect on heat diffusion, making a constructive contribution to heat transfer. An examination of the local Nusselt number at the bottom wall, as seen in Fig. 10, reveals a clear surge in heat transfer rate particularly at the rightmost regions of the bottom wall, for smaller nanoparticle fusion temperatures.

Fig. 11 also shows that the nanoparticle fusion temperature imparts

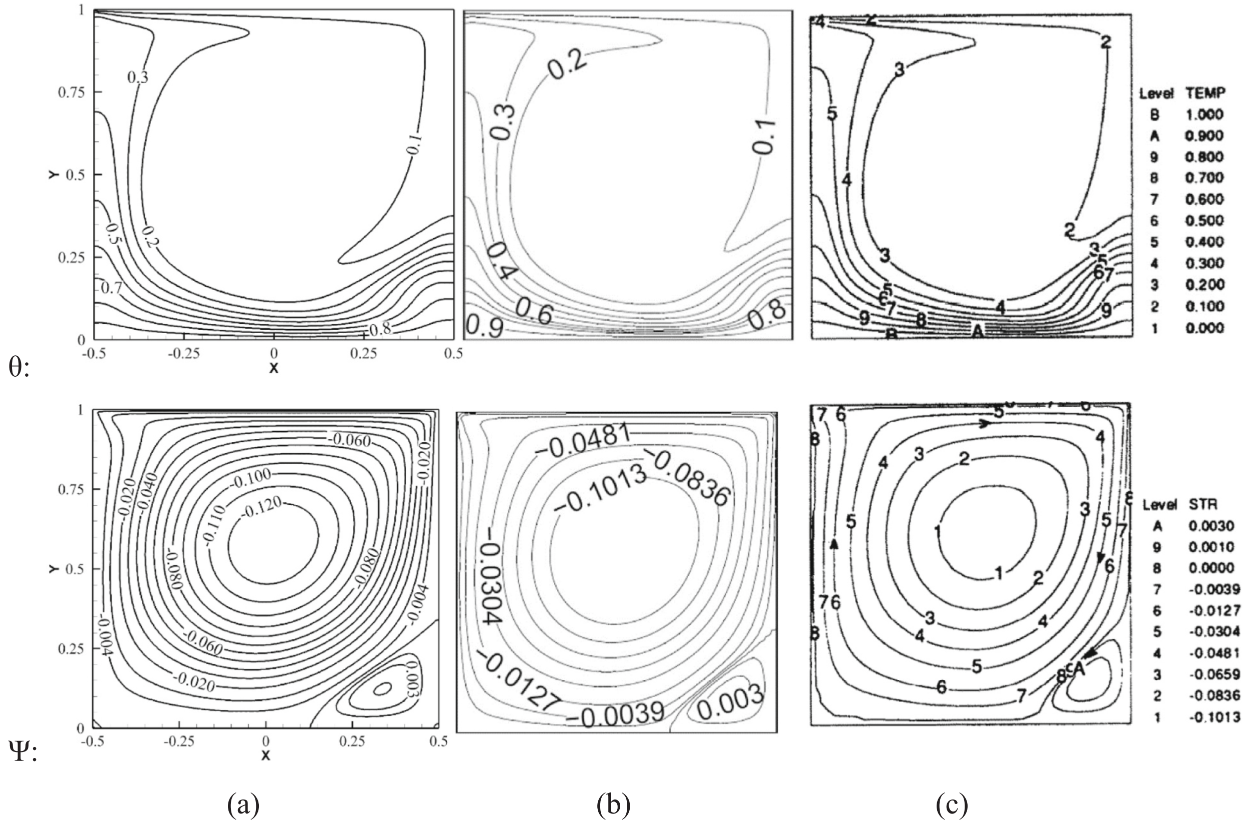

Fig. 5. Comparison of isotherms and streamlines for a lid-driven cavity at the top with a cold wall at the top, a heated wall at the bottom, and insulated side walls when $Re = 500$, $Pr = 1.0$, and Ri = 0.4: (a) the present study, (b) study of Moallemi and Jang [73], and Roy et al. [64].

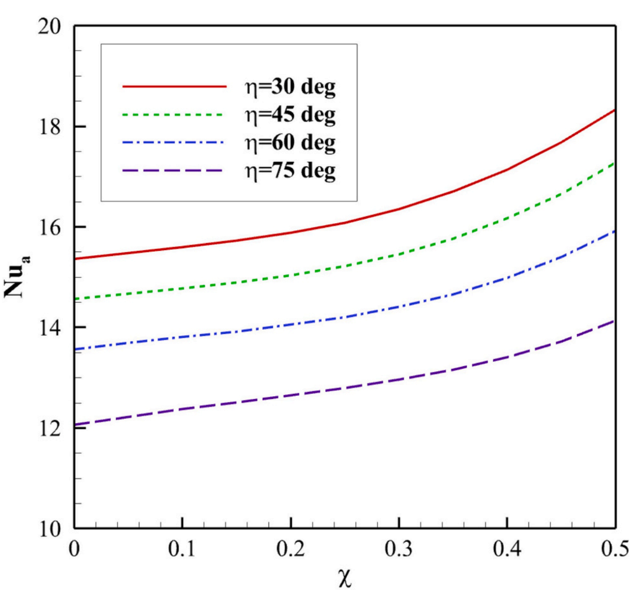

Fig. 6. Impact of geometrical parameter (χ) and trapezoidal angle (η) on the Nu_a.

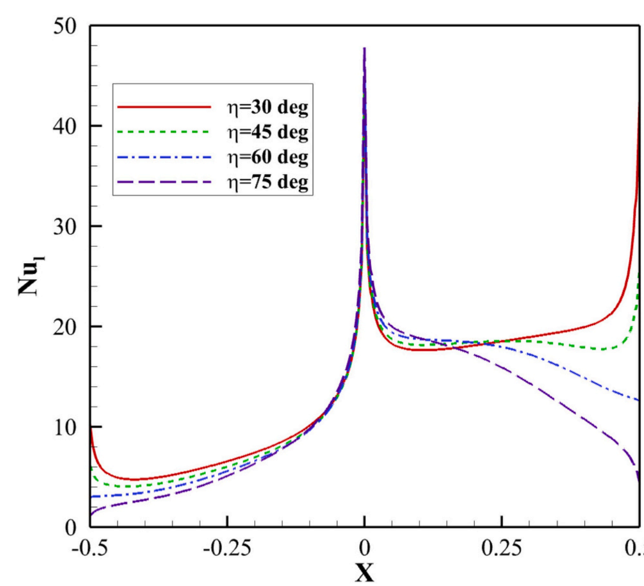

Fig. 7. Influence of trapezoidal angles on Local Nusselt number $\eta = 60^\circ$ $\eta = 75^\circ$.

only a negligible impact on the streamlines. In essence, the phase change of nanoparticles primarily tweaks the local heat capacity of the nanofluid, rather than significantly altering the fluid flow circulations. For the case of Ri = 1.0 and $\theta_{fu} = 0.2$, a peak Nu_a value of 14.5 can be observed. However, for the same Ri of 1.0, boosting the fusion temperature to 0.9 results in a slight drop in Nu_a, registering at 13.6. This underlines that the strategic selection of nanoparticle fusion temperature could potentially enhance heat transfer efficiency by approximately 6%.

The shift of the optimum fusion temperature can be explained by the asymmetric coupling between the lid-driven circulation and the phase-change zone. In the present configuration, the top cold wall moves horizontally and generates a dominant clockwise circulation. This forced motion continuously transports colder fluid along the upper part

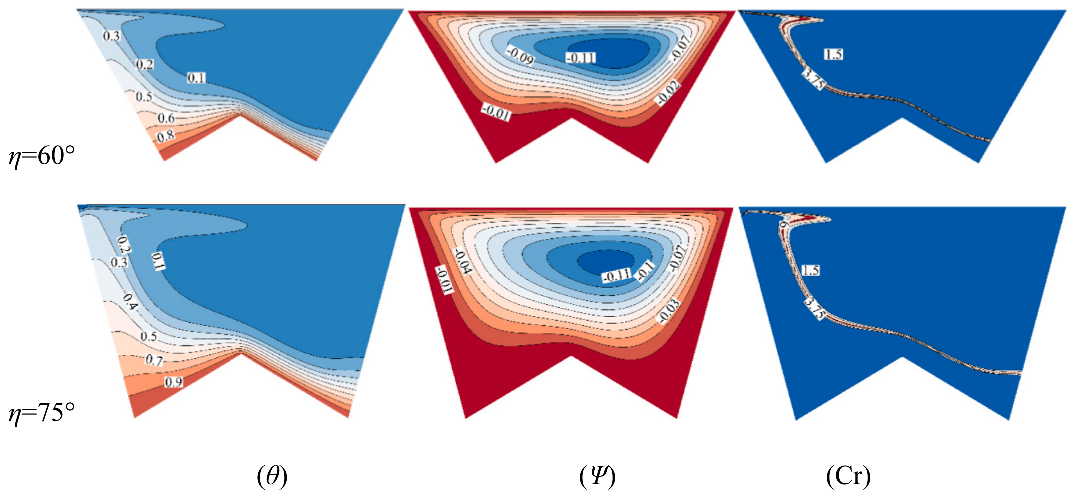

Fig. 8. Isotherms, streamlines, and the heat capacity ratio maps (Cr) for two trapezoidal angles $\eta = 60^{\circ}$ and $\eta = 75^{\circ}$.

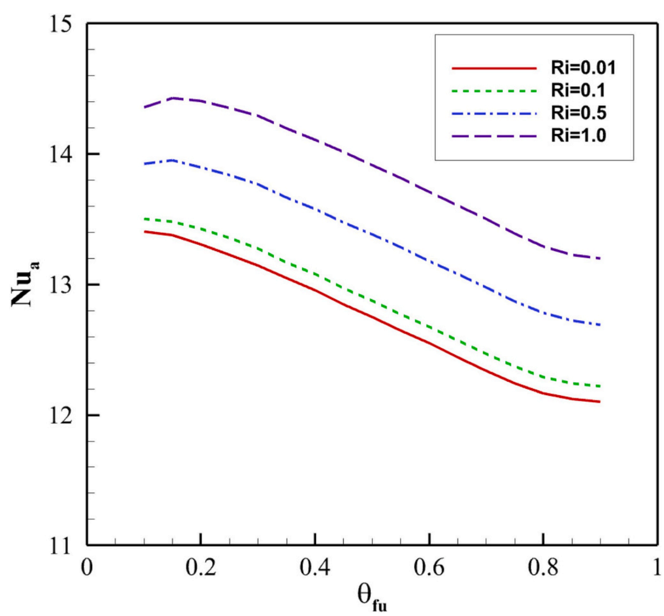

Fig. 9. Impact of Richardson number and nanoparticles fusion temperature on Nu_a.

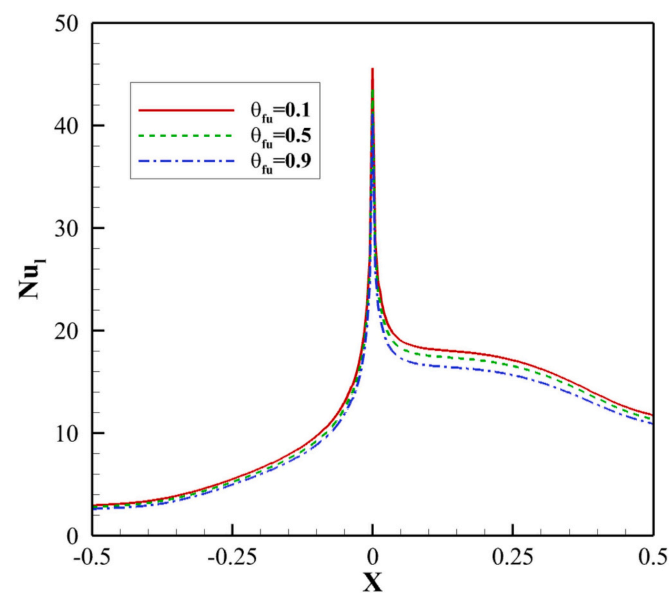

Fig. 10. Effect of fusion temperature on Local Nusselt number $\theta_{fu} = 0.1$: $\theta_{fu} = 0.5$: $\theta_{fu} = 0.9$:

of the enclosure and then redirects it toward the heated W-shaped wall. As a result, the strongest convective exchange is not symmetrically distributed around the enclosure center, unlike in many pure natural-convection cavities. Instead, the most effective heat removal path is linked to the moving cold lid and the recirculating flow generated by it.

The heat-capacity-ratio contours in Fig. 11 show where the NEPCM particles are undergoing phase change. At lower fusion temperatures, especially around $\theta_{fu} \approx 0.2$, the phase-change region overlaps more effectively with the lid-driven convective path. In this situation, the capsules absorb latent heat near the heated region and release or redistribute it along the high-advection path toward the cold moving wall. Therefore, the latent heat capacity of the NEPCM suspension is used more efficiently. By contrast, when θ_{fu} is increased toward 0.5 or 0.9, the phase-change region moves closer to the hotter lower region and becomes less aligned with the main convective transport path. In that case, the latent heat contribution is more localized and has a weaker influence on the overall heat removal from the W-shaped wall.

This interpretation is also supported by the streamline maps in Fig. 11, which show that changing θ_{fu} has only a weak influence on the global flow structure. Therefore, the change in Nu_a with fusion temperature is mainly a thermal-storage effect rather than a hydrodynamic effect. The optimal value near $\theta_{fu} \approx 0.2$ is thus a consequence of matching the phase-change temperature range with the asymmetric temperature field generated by the moving cold lid and the W-shaped heated wall.

Fig. 12 provides a detailed depiction of the combined effects of nanoparticle concentration and fusion temperature on the heat transfer rate, represented by the Nusselt number, Nu_a. Close examination of the diagram indicates a distinct pattern: as the nanoparticle concentration elevates, there is a notable enhancement in the Nu_a. Moreover, this finding is consistent with the observations made in Fig. 9, which demonstrated that elevating the nanoparticle fusion temperature has an inverse effect, thereby reducing the heat transfer rate (Nu_a). Using 5% of nanoparticles, at a fusion temperature of 0.2, provides $Nu_a = 13.9$. This is while a zero concentration of nanoparticles provides $Nu_a = 7.5$.

When the nanoparticle concentration is increased, the underlying mechanism increases the thermal conductivity and latent heat capacity of the nanofluid. This elevated thermal performance helps facilitate the transfer of thermal energy, thus enhancing the overall heat transfer

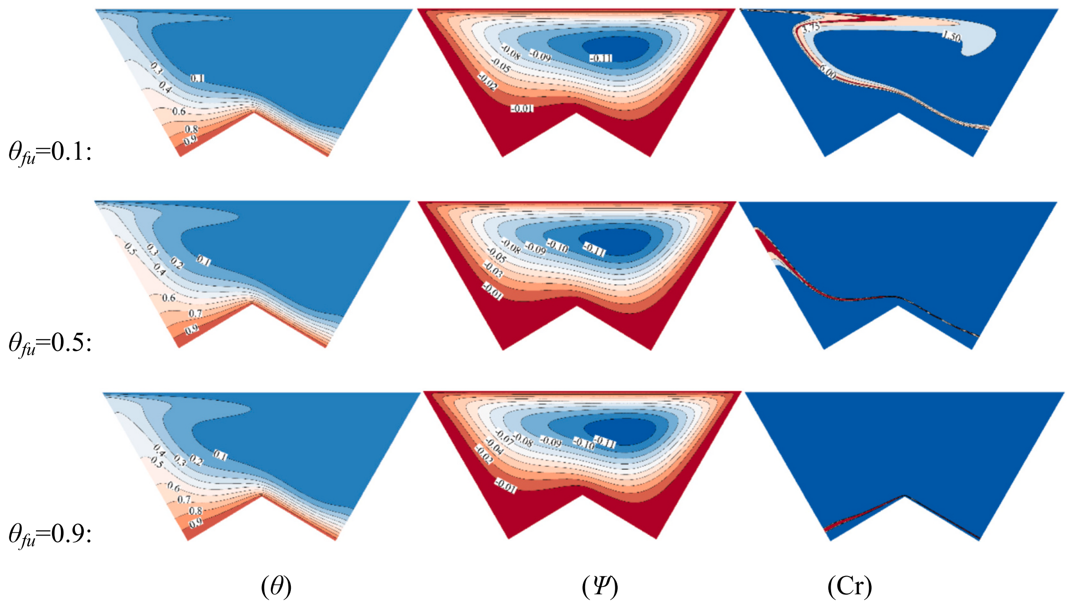

Fig. 11. Isotherms, streamlines, and the heat capacity ratio maps (Cr) for three fusion temperatures $\theta_{fu} = 0.1$, $\theta_{fu} = 0.5$, and $\theta_{fu} = 0.9$.

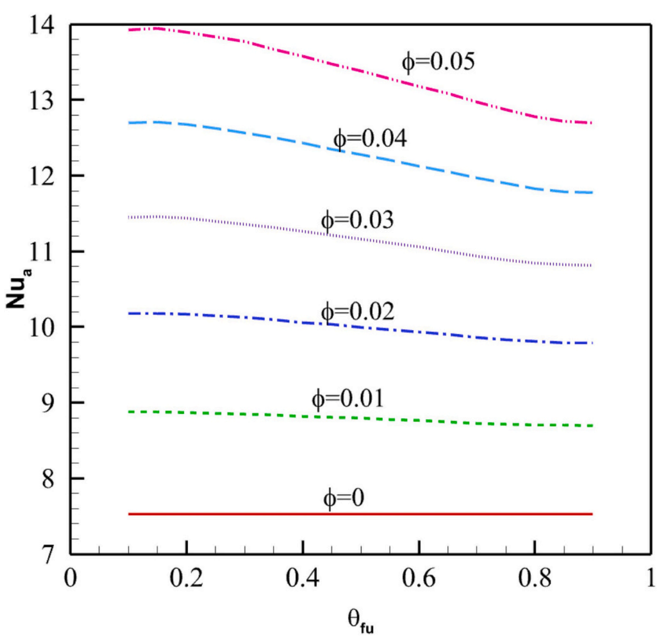

Fig. 12. Impact of concentration (ϕ) and fusion temperature (θ_{fu}) on Nu_a.

process. Interestingly, there seems to be a certain sweet spot for maximizing heat transfer efficiency. When the nanoparticle fusion temperature hovers around $\theta_{fu} = 0.2$, the heat transfer rate attains its peak, underscoring the importance of the careful calibration of the fusion temperature in order to optimize the heat transfer. As seen, NEPCM particles provide 46% heat transfer enhancement.

The reported enhancement should be interpreted together with the corresponding viscosity penalty. According to Eq. (15), increasing the NEPCM concentration to $\phi = 0.05$ increases the effective viscosity ratio to $\mu_b/\mu_f = 1.625$. Therefore, although the modified average Nusselt number increases because of the combined effect of higher effective thermal conductivity and latent heat storage, the suspension also becomes more viscous. In an actual device, this may increase the mechanical power required to maintain the lid motion or to circulate the suspension. Since the present configuration is a closed lid-driven enclosure rather than an inlet–outlet channel, pressure drop and pumping power are not directly defined in the present formulation. Thus, the 46% increase in Nu_a should be understood as a heat-transfer enhancement under prescribed lid-velocity, not as a complete thermo-hydraulic performance index. Future work should combine the present heat-transfer analysis with lid-driving power, entropy generation, and experimental suspension-stability measurements.

Previous research on the natural convection of NEPCM suspension in geometrically uniform settings, such as a square cavity with heated walls [77] or objects heated symmetrically [17], suggested an optimal fusion temperature near $\theta_{fu} = 0.5$. This finding was attributed to the symmetrical nature of the physical models and their boundary conditions. In contrast, the current study introduces the complexity of mixed convection, prompted by a lid-driven top wall, and the non-uniform shape of the enclosure, disrupting these symmetries. Consequently, the optimal fusion temperature has been observed to shift toward the cold moving

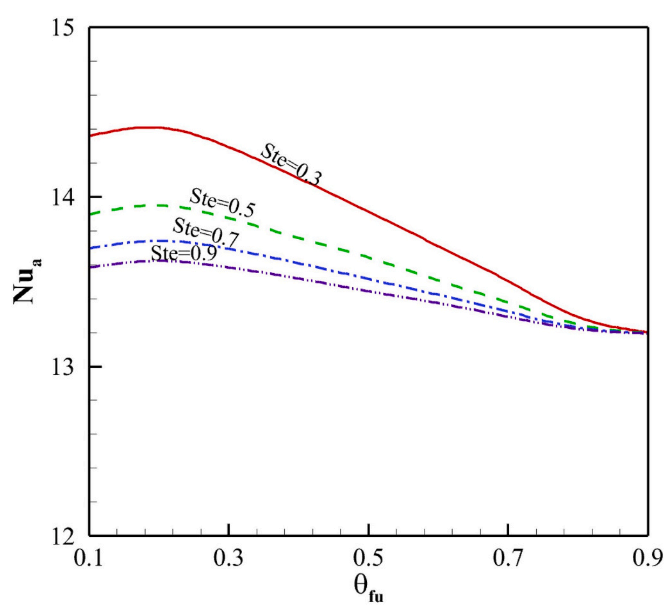

Fig. 13. Nu_a as a function of Stefan number (Ste) and NEPCM fusion temperature (θ_{fu}).

wall, which features more heat transfer potential due to the strong advection effects. Fig. 13 illustrates the influence of Stefan number on the heat transfer rate. As Ste. increases Nu_a reduces. An increase of Ste. means lower rate of phase change energy transport and thus lower heat transfer rate. The highest heat transfer rate can be observed about a fusion temperature of 0.2, which is in agree with the results of Figs. 9 and 12.

The above trends should be interpreted within the investigated parameter ranges. The present study is restricted to dilute NEPCM suspensions, $0 \le \phi \le 0.05$, laminar flow with $Re = 100$, $0.001 \le Ri \le 1.0$, $30^\circ \le \eta \le 90^\circ$, $0 \le \chi \le 0.5$, and $0.1 \le \theta_{fu} \le 0.9$. Therefore, the identified optimum fusion temperature and the reported 46% heat-transfer enhancement should not be extrapolated to higher particle concentrations, turbulent flow, different capsule materials, temperature-dependent property models, or three-dimensional configurations without additional simulations or experiments. The ANN and RSM surrogates are also used only for interpolation inside this domain.

$$\mathrm{Nu_a} = a_0 + a_1 \times (\eta/\eta_0) + a_2 \times (\chi/\chi_0) + a_3 \times (\phi/\phi_0) + a_4 \times (\theta_{fu}/\theta_{fu,0}) + a_5 \times (\mathrm{Ri}/\mathrm{Ri}_0) \tag{34}$$

where the coefficients are given by: $a_0 = 10.0103$, $a_1 = -3.7211$, $a_2 = 1.1132$, $a_3 = 2.9805$, $a_4 = -0.4220$, $a_5 = 0.5125$. The quadratic RSM was expressed in coded variables as:

$$Nu_{a,\mathrm{RSM}} = b_0 + \sum_{i=1}^{5} b_i X_i + \sum_{i=1}^{5} b_{ii} X_i^2 + \sum_{i<j} b_{ij} X_i X_j \tag{35}$$

where X_i denotes the coded form of the five input variables. The model contains 21 fitted coefficients: one intercept, five linear coefficients, five squared coefficients, and ten two-way interaction coefficients. Thus, Eq. (35) after the fit computations can be written as:

$$\begin{aligned} Nu_{a,\mathrm{RSM}} = {} & 10.3547536 - 2.011058631\eta + 0.9379963395\chi + 2.864679252\phi \\ & -0.3016729144\theta_{fu} + 0.5211987887\mathrm{Ri} - 0.4369499314\eta^2 \\ & -0.3479132722\eta\chi - 0.6144980116\eta\phi + 0.05466910058\eta\theta_{fu} \\ & +0.1785426805\eta\mathrm{Ri} + 0.5228573552\chi^2 + 0.3698300866\chi\phi \\ & -0.03549194156\chi\theta_{fu} - 0.2048267538\chi\mathrm{Ri} - 0.1281323588\phi^2 \\ & -0.339428111\phi\theta_{fu} + 0.05715554653\phi\mathrm{Ri} - 0.02292119309\theta_{fu}^2 \\ & +0.017468785680\theta_{fu}\mathrm{Ri} - 0.06183475965\mathrm{Ri}^2. \end{aligned} \tag{36}$$

5. Neural network analysis

The FEM model was used as the reference numerical solver for the governing conservation equations. However, repeated FEM simulations are computationally expensive when rapid interpolation, parameter screening, or optimization is required within the investigated design space. Therefore, the artificial neural network was not introduced as a replacement for the FEM solution. Instead, it was used as a compact nonlinear surrogate model for predicting the modified average Nusselt number, Nu_a, from the five control parameters: η, χ, ϕ, θ_{fu}, and *Ri*.

Here a linear correlation in Eq. (34) was computed and used as the first-order engineering baseline. A conventional quadratic response surface model (RSM) was also constructed as an interpretable nonlinear baseline. The three models, namely the linear Eq. (34), the quadratic RSM, and the ANN, were evaluated using the same FEM-generated dataset and the same train/validation/test partitions.

The dataset consisted of 2148 FEM-generated cases. The dataset can be accessed here: http://doi.org/10.17632/wdzs4bw4nm.1

Each case included the trapezoidal angle η, W-wall shape factor χ, NEPCM particle concentration ϕ, dimensionless fusion temperature θ_{fu}, Richardson number *Ri*, and the FEM-computed modified average Nusselt number Nu_a. The angle was converted to degrees before applying the linear correlation because Eq. (34) uses $\eta/60$ with η expressed in degrees. To reduce data leakage, a group-aware train/validation/test split was used. Rows with the same exact input combination were kept in the same subset. The final split used 70% of the input groups for training, 15% for validation, and 15% for testing.

The mid-range of each parameter was determined and used for normalization: $\eta_0 = 60^\circ$, $\chi_0 = 0.25$, ϕ=0.025, $\theta_{fu,0} = 0.5$, $\mathrm{Ri}_0 = 0.505$. Upon scaling the input parameters around these mid-ranges, a linear fit was employed. The resulting relationship is captured as:

This RSM was included to test whether a standard nonlinear response surface can reproduce the FEM data with accuracy comparable to the ANN. The ANN architecture was selected to be compact rather than excessively deep. It consisted of five input neurons, one dense layer with 3 neurons, three dense hidden layers with 8 neurons each, and one linear output neuron, giving a 5–3–8-8-8-1 architecture as shown in Fig. 14. The hidden layers used the hyperbolic tangent activation function. The network contained 203 trainable parameters, which is small compared with the 2148 FEM-generated samples. Training was performed using the Adam optimizer with a learning rate of 0.01. The selected ANN was trained for 20,000 epochs, and the best validation performance occurred at epoch 19,923.

Table 6 compares the predictive performance of the linear Eq. (34), the quadratic RSM Eq. (36), and the dense ANN. All errors are reported in the original Nu_a scale. The linear Eq. (34) gives a test RMSE of 0.567579 and $R^2 = 0.962434$. The quadratic RSM substantially improves the prediction accuracy, with a test RMSE of 0.080910 and $R^2 = 0.999237$. The dense ANN gives the lowest average prediction error, with a test MAE of 0.045014, test RMSE of 0.068487, test MAPE of 0.405%, and $R^2 = 0.999453$. Therefore, the ANN reduces the test RMSE by approximately 87.9% compared with the linear Eq. (34), and by approximately 15.4% compared with the quadratic RSM. The RSM has a slightly smaller maximum absolute error than the ANN; therefore, the ANN is not claimed to be superior in every individual metric. Rather, it is retained because it gives the lowest average error and the highest coefficient of determination on the independent test set.

The comparison shows that the linear Eq. (34) is useful as a transparent first-order correlation, while the RSM and ANN capture the nonlinear response more accurately; the ANN gives the lowest average test error, whereas the RSM gives the smallest maximum absolute error.

Fig. 15 provides the corresponding parity plots for the three models. The linear Eq. (34) shows visible scatter and systematic deviations from

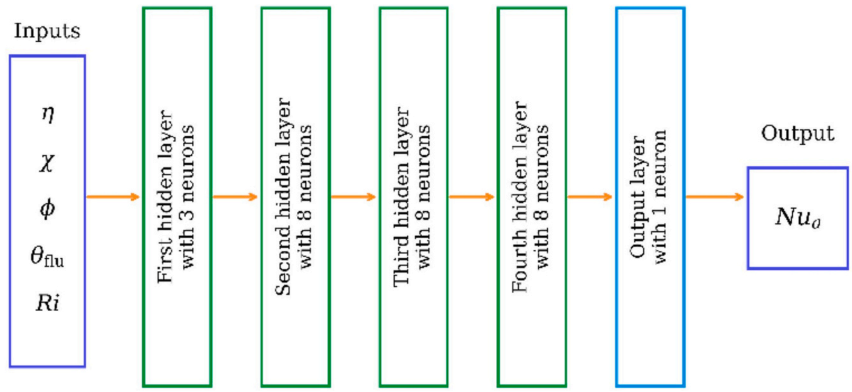

Fig. 14. Dense neural network design to find the relationship between non-dimensional model parameters and Nu_a. There are five input parameters to the neural network and one output parameter.

Table 6
Comparative predictive performance of the linear correlation, quadratic RSM, and dense ANN for predicting the FEM-computed modified average Nusselt number Nu_a. All errors are evaluated in the original Nu_a scale. The test set was obtained using a group-aware split to prevent repeated input combinations from appearing simultaneously in the training and test subsets.

Metric	Linear correlation, Eq. (34)	Quadratic RSM Eq. (36)	Dense ANN
Parameters	6 fitted coefficients	21 fitted coefficients	203 trainable parameters
Train RMSE	0.542102	0.093982	0.060825
Validation RMSE	0.525763	0.091431	0.061874
Test MAE	0.424206	0.062024	0.045014
Test RMSE	0.567579	0.080910	0.068487
Test MSE	0.322146	0.006546	0.004690
Test MAPE (%)	4.05244	0.590661	0.405312
Test R^2	0.962434	0.999237	0.999453
Test MaxAE	1.93311	0.258804	0.301734

the diagonal line, indicating that a first-order equation cannot capture all curvature and interaction effects in the FEM-generated response. The RSM and ANN predictions are much more closely aligned with the FEM values, confirming the importance of nonlinear and interaction terms. The ANN provides the tightest overall agreement with the FEM results in terms of average error. Fig. 16. provides the Residual distributions on the independent test set for Eq. (34), RSM, and ANN.

To further interpret the ANN surrogate, a permutation-importance analysis was performed. The particle concentration ϕ was the dominant input, contributing 47.7% of the relative importance, followed by the trapezoidal angle η at 21.0% and the W-wall shape factor χ at 19.9%. The Richardson number and fusion temperature contributed 6.0% and 5.4%, respectively. This ranking is physically consistent with the FEM results because NEPCM concentration directly modifies the effective thermal conductivity and latent heat capacity of the suspension, while the enclosure angle and W-wall shape factor control the circulation path and thermal boundary-layer development.

After validation, the trained ANN was used to generate additional contour maps for rapid design-space exploration within the investigated parameter ranges. The ANN was used only for interpolation inside these ranges, and no extrapolation outside the studied intervals is claimed. Subsequently, this well-trained neural network was applied to assess how the fusion temperature and nanoparticle concentration influence Nu_a. By analyzing over 4000 simulation cases with this dense neural network, we mapped the relationship between the fusion temperature (θ_{fu}) and nanoparticle concentration (ϕ) onto a contour map, as shown in Fig. 17. The results indicate that increasing the nanoparticle concentration enhances the heat transfer rate. However, raising the fusion temperature reduces the heat transfer rate, particularly at higher concentrations, due to the greater number of nanoparticles aiding in heat transfer.

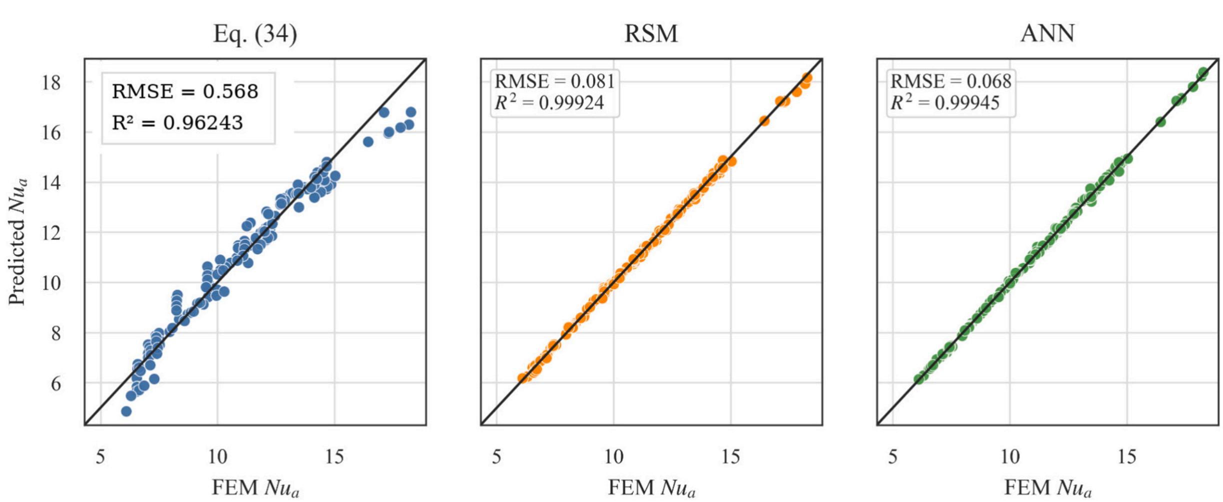

Fig. 15. Parity plots comparing FEM-computed Nu_a and model-predicted Nu_a on the independent test set for the linear correlation, Eq. (34), the quadratic RSM Eq. (36), and the dense ANN. The diagonal line represents perfect prediction. The linear model shows visible systematic deviations, whereas the RSM and ANN predictions are closely aligned with the FEM results.

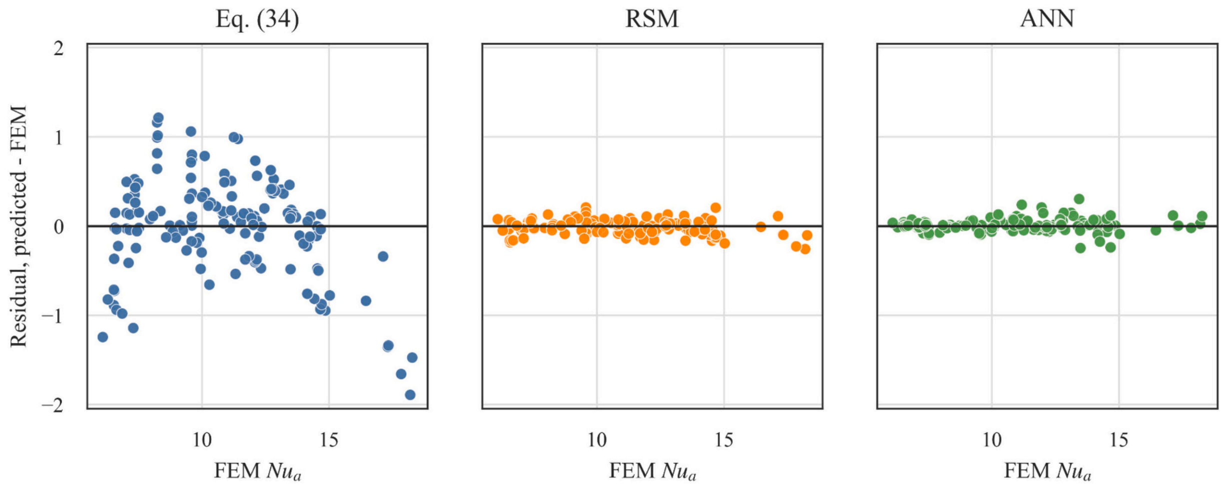

Fig. 16. Residual distributions on the independent test set for Eq. (34), RSM, and ANN, where the residual is defined as Nu_a, predicted - Nu_a, FEM. The residuals of Eq. (34) show larger dispersion and systematic trends, while the RSM and ANN residuals are concentrated near zero.

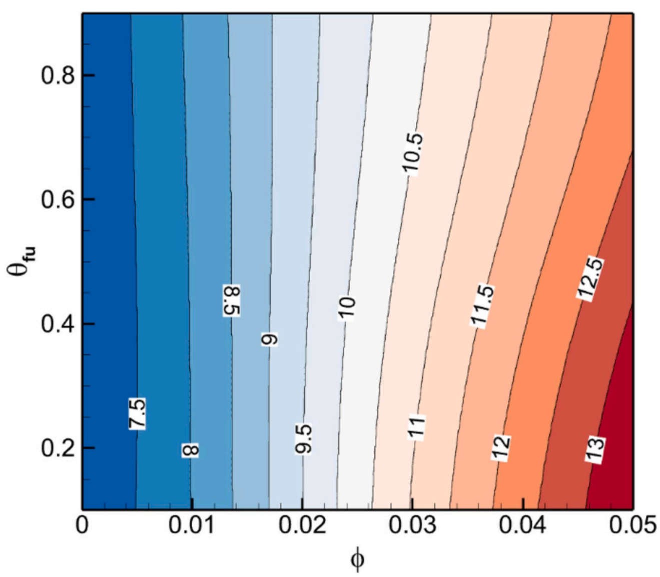

Fig. 17. Contours of fusion temperature against nanoparticles concentration for Nu_a when $\eta = 60^\circ$, Ri = 0.1, and $\chi = 0.3$.

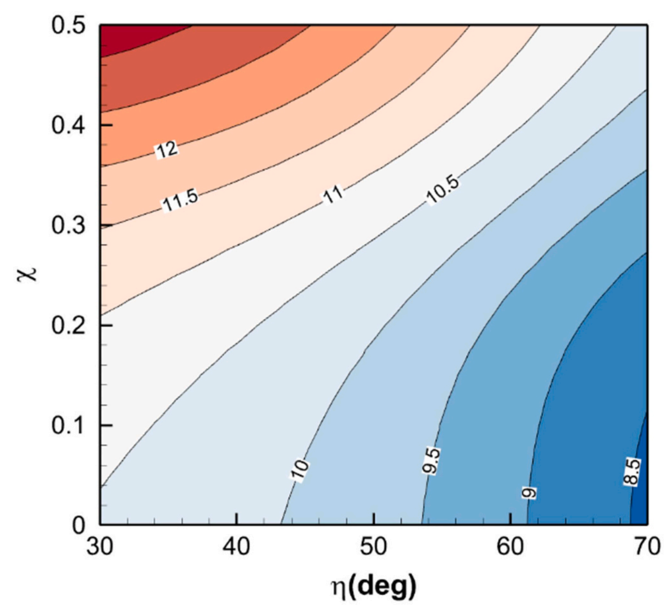

Fig. 18. Contours of η against χ concentration for Nu_a when Ri = 0.1, ϕ = 0.025, and $\theta_{fu} = 0.9$.

Fig. 18 examines the effects of enclosure angle (η) and the bottom wall shape factor (χ) on the heat transfer rate (Nu_a). It reveals that decreasing η or increasing χ leads to higher heat transfer rates. The influence of χ becomes more pronounced at higher values of η, and vice versa, indicating a synergistic effect on heat transfer. The highest heat transfer can be observed for the smallest angle η. Additionally, at $Nu_a = 11$, we observe a noticeable change in the contour lines' non-linearity, suggesting complex interactions between these parameters and heat transfer. This comprehensive analysis underscores the neural network's capability to accurately predict heat transfer rates and elucidate the significant impact of various parameters on Nu_a. Considering a fair shape factor $\chi = 0.3$, the variation of enclosure angle from $\eta = 70$ to $\eta = 30$, increases the heat transfer rate from 9.5 to 11.5, which is about 17.3% improvement in the heat transfer rate.

6. Conclusions

The current research meticulously explores the dynamics of mixed convection within a trapezoidal cavity filled with water and NEPCM. The study elucidates how nanoparticles, consisting of a PCM core and a polyurethane (PU) shell, operate within the cavity. The research scrutinizes the effect of several parameters such as nanoparticle concentration, enclosure geometrical parameters, trapezoidal angle, nanoparticle fusion temperature, and the Richardson number on the heat transfer rate (Nu_a). The FEM was applied to simulate the phase change heat transfer of NEPCM suspension in the enclosure. The results confirm that an elevation in nanoparticle concentration enhances the thermal conductivity and latent heat capacity of the nanofluid, thus accelerating the heat transfer rate. Using 5% of NEPCM particles results in a 46% heat transfer enhancement compared to a pure host fluid. This enhancement is obtained under prescribed lid velocity and should be balanced against the viscosity increase of the suspension; therefore, future engineering assessments should include lid-driving power or pumping-power penalties and suspension-stability constraints.

Results demonstrate a peak Nu_a value of 14.5 for a Richardson number of 1.0 and nanoparticle fusion temperature (θ_{fu}) of 0.2. However, an increase in θ_{fu} to 0.9, under the same Richardson number, incurs a minor reduction in Nu_a to 13.6. This suggests that a judicious selection of nanoparticle fusion temperature could potentially increase heat transfer efficiency by approximately 6%.

The study also reveals the effect of the trapezoidal angle and the geometrical parameter of the W-wall on the modified average Nusselt number. The results show that increasing these parameters drives the heated wall toward the cold top wall, increasing the fluid velocity near the W-wall and therefore boosting the heat transfer rate. The optimum case for the highest heat transfer rate corresponds to the low fusion temperature ($\theta_{fu} \sim 0.2$), lowest cavity angle (η), highest bottom wall shape factor (χ), and also highest Richardson number (Ri).

The surrogate-model comparison further showed that the ANN contribution is not limited to post-processing visualization. The recomputed linear correlation, Eq. (34), remains useful as a transparent first-order engineering estimate, but its test RMSE was 0.5676. The quadratic RSM reduced the test RMSE to 0.0809, while the compact ANN reduced it further to 0.0685 and produced the highest test R^2 of 0.999453. Therefore, the ANN provides the most accurate average interpolation surrogate among the tested models within the investigated FEM parameter space. However, the RSM had a slightly smaller maximum absolute error, so the ANN should be interpreted as the best average-error surrogate rather than as a model that dominates every metric.

The comprehensive analysis and the derived insights significantly enrich their understanding of the heat transfer process within trapezoidal enclosures. It underscores the key role played by nanoparticles and their fusion temperature in optimizing heat transfer rates. These findings hold significant implications for applications across a wide array of fields including electronics cooling, thermal storage, and heat exchanger design.

CRediT authorship contribution statement

Rawia Ahmed: Writing – original draft, Software, Resources, Investigation, Formal analysis, Conceptualization. **Hanene Guesmi:** Writing – review & editing, Writing – original draft, Visualization, Validation, Resources. **Hany Alalfy:** Writing – original draft, Project administration, Methodology, Investigation. **Jehan Habib:** Writing – review & editing, Writing – original draft, Resources, Funding acquisition, Data curation. **Jana Shafi:** Writing – original draft, Visualization, Software, Project administration, Data curation. **Khalil Hajlaoui:** Writing – review & editing, Writing – original draft, Visualization, Validation, Project administration, Methodology. **Mehdi Ghalambaz:** Writing – review & editing, Writing – original draft, Validation, Supervision, Project administration, Formal analysis.

Declaration of competing interest

The authors declare that they have no known competing financial interests or personal relationships that could have appeared to influence the work reported in this paper.

Acknowledgements

This research has been funded by Scientific Research Deanship at University of Ha'il - Saudi Arabia through project number RG-25 100.

Appendix A: Derivation of the non-dimensional governing equations

In this study, the governing equations are expressed in dimensionless form through appropriate scaling.

Continuity equation.

In Eq. (1), the variables are replaced with scaled variables according to the continuity equation, as shown in Eq. (A1):

$$\left(\frac{\partial(UU_t)}{\partial(XH)}+\frac{\partial(VU_t)}{\partial(YH)}\right)=0 \tag{A1}$$

The constant values emerge from the process of differentiation, as indicated:

$$\left(\frac{U_t}{H}\right)\left(\frac{\partial U}{\partial X}+\frac{\partial V}{\partial Y}\right)=0 \tag{A2}$$

It is known that the first term, U_t/H, is not zero, leading to the conclusion that the second term must be zero, which leads to Eq. (18).

Momentum equations.

To address the x-momentum equation, the scaled parameters are substituted into Eq. (2), resulting in an equation that includes constant values:

$$\rho_b UU_t\frac{\partial(UU_t)}{\partial(XH)}+\rho_b VU_t\frac{\partial(UU_t)}{\partial(YH)}=-\frac{\partial(P\rho_f U_t^2)}{\partial(XH)}+\mu_b\left(\frac{\partial^2(UU_t)}{\partial(XH)^2}+\frac{\partial^2(UU_t)}{\partial(YH)^2}\right) \tag{A3}$$

These constants are then taken out of the differentiation process, yielding a new equation:

$$\frac{\rho_b UU_t^2}{H}\frac{\partial U}{\partial X}+\frac{\rho_b VU_t^2}{H}\frac{\partial U}{\partial Y}=-\frac{\rho_f U_t^2}{H}\frac{\partial P}{\partial X}+\mu_b\frac{U_t}{H^2}\left(\frac{\partial^2 U}{\partial X^2}+\frac{\partial^2 U}{\partial Y^2}\right) \tag{A4}$$

Next, the equation is multiplied by $\frac{H}{\rho_f U_t^2}$ and the definition of the Reynolds number $Re=\frac{\rho_f U_t H}{\mu_f}$ is used to reach Eq. (19).

For the y-momentum equation, the scaled parameters are inserted into Eq. (3):

$$\begin{aligned}&\rho_b(UU_t)\frac{\partial(VU_t)}{\partial(XH)}+\rho_b(VU_t)\frac{\partial(VU_t)}{\partial(YH)}=-\frac{\partial(P\rho_f U_t^2)}{\partial(YH)}+\\&\mu_b\left(\frac{\partial^2(VU_t)}{\partial(XH)^2}+\frac{\partial^2(VU_t)}{\partial(YH)^2}\right)+g\rho_b\beta_b(\theta\Delta T+T_c-T_c)\end{aligned} \tag{A5}$$

and the constant values are extracted from the differentiation process:

$$\rho_b\frac{U_t^2}{H}U\frac{\partial V}{\partial X}+\rho_b\frac{U_t^2}{H}V\frac{\partial V}{\partial Y}=-\frac{\rho_f U_t^2}{H}\frac{\partial P}{\partial Y}+\mu_b\frac{U_t}{H^2}\left(\frac{\partial^2 V}{\partial X^2}+\frac{\partial^2 V}{\partial Y^2}\right)+g\rho_b\beta_b(\theta\Delta T) \tag{A6}$$

The resulting equation is then multiplied by $\frac{H}{\rho_f U_t^2}$:

$$\left(\frac{\rho_b}{\rho_f}\right)\left(U\frac{\partial V}{\partial X}+V\frac{\partial V}{\partial Y}\right) = -\frac{\partial P}{\partial Y}+\frac{\mu_b}{\rho_f}\frac{1}{U_t H}\left(\frac{\partial^2 V}{\partial X^2}+\frac{\partial^2 V}{\partial Y^2}\right)+\frac{H}{\rho_f U_t^2} g\rho_b\beta_b(\theta\Delta T) \tag{A7}$$

By utilizing the definitions of the Reynolds number and the Grashof number ($Gr = \rho_f^2 g\beta_f \Delta T H^3/\mu_f^2$), the above equation can be re-written as:

$$\begin{aligned}&\left(\frac{\rho_b}{\rho_f}\right)\left(U\frac{\partial V}{\partial X}+V\frac{\partial V}{\partial Y}\right) = -\frac{\partial P}{\partial Y}+\frac{1}{\mathrm{Re}}\left(\frac{\mu_b}{\mu_f}\right)\left(\frac{\partial^2 V}{\partial X^2}+\frac{\partial^2 V}{\partial Y^2}\right)+\\ &\left(\frac{H^2}{H^2}\right)\left(\frac{\mu_f^2}{\mu_f^2}\right)\left(\frac{\rho_f}{\rho_f}\right)\frac{(\rho\beta)_f}{(\rho\beta)_f}\frac{H}{\rho_f U_t^2} g\rho_b\beta_b(\theta\Delta T)\end{aligned} \tag{A8}$$

where can be further simplified by using non-dimensional parameters to Eq. (20).

Heat Equation.

Moving on to the heat equation, the scale parameters are inserted into Eq. (4):

$$(\rho C_p)_b(U_t U)\frac{\partial(\theta\Delta T+T_c)}{\partial(XH)}+(\rho C_p)_b(U_t V)\frac{\partial(\theta\Delta T+T_c)}{\partial(YH)} = k_b\left(\frac{\partial^2(\theta\Delta T+T_c)}{\partial(XH)^2}+\frac{\partial^2(\theta\Delta T+T_c)}{\partial(YH)^2}\right) \tag{A9}$$

By removing the fixed values from differentiation and considering that the differentiation of Tc is zero, a new equation is obtained:

$$(\rho C_p)_b U_t\frac{\Delta T}{H}U\frac{\partial\theta}{\partial X}+(\rho C_p)_b U_t\frac{\Delta T}{H}V\frac{\partial\theta}{\partial Y} = k_b\frac{\Delta T}{H^2}\left(\frac{\partial^2\theta}{\partial X^2}+\frac{\partial^2\theta}{\partial Y^2}\right) \tag{A10}$$

Multiplying both sides of the equation by $\frac{H}{(\rho C_p)_f U_t \Delta T}$ and simplifying the equation yields:

$$\frac{(\rho C_p)_b}{(\rho C_p)_f}\left(U\frac{\partial\theta}{\partial X}+V\frac{\partial\theta}{\partial Y}\right) = \left(\frac{k_f}{k_f}\right)\left(\frac{\nu_f}{\nu_f}\right)\left(\frac{\rho_f}{\rho_f}\right)\frac{k_b}{(\rho C_p)_f}\frac{1}{U_t}\frac{1}{H}\left(\frac{\partial^2\theta}{\partial X^2}+\frac{\partial^2\theta}{\partial Y^2}\right) \tag{A11}$$

Using the definition of Reynolds number and Prandtl number ($Pr = \nu_f/\alpha_f$) where $\alpha_f = k_f/(\rho C_p)_f$ and $\nu_f = \mu_f/\rho_f$, the above equation can be re-written as Eq. (23).

Appendix B: Non-dimensional form of boundary conditions

In the derivation of the non-dimensional form of the boundary conditions, the scale parameters are inserted into Eq. (5) for the bottom wall:

$$U_t U = U_t V = 0, \frac{T-T_c}{\Delta T} = \frac{T_h - T_c}{\Delta T} \tag{B1}$$

By recognizing that U_t is non-zero, the hydraulic and thermal conditions for the bottom wall are obtained as Eq. (27). Similarly, for the top wall, the scale parameters are inserted into Eq. (6), yielding an equation that represents the top wall:

$$U_t U = U_t, U_t V = 0, \frac{T-T_c}{\Delta T} = \frac{T_c - T_c}{\Delta T} \tag{B2}$$

By noting that U_t is non-zero, the hydraulic and thermal conditions are obtained as Eq. (28). Lastly, for the side walls, the given equation is rearranged and expressed in the specified form

$$U_t U = U_t V = 0, \frac{\partial(\theta\Delta T+T_c)}{\partial(HN)} = 0 \tag{B3}$$

By applying the deferential operator, the equation can be simplified as:

$$U_t U = U_t V = 0, \frac{\Delta T}{H}\frac{\partial\theta}{\partial N} = 0 \tag{B4}$$

whereby noting U_t and $\Delta T/H$ are non-zero, the above equation leads to Eq. (29).

Data availability

Research Link Provided

Dataset: Neural network-finite element study of heat transfer enhancement of nano-encapsulated phase change materials suspensions in a lid-driven trapezoid cavity (Original data) (Mendeley Data)

References

[1] R. Hidki, L. El Moutaouakil, M. Boukendil, Z. Charqui, Z. Zrikem, Mixed-convection coupled with thermal-radiation in a ventilated horizontal channel containing different electronic components, J. Thermophys. Heat Transf. (2023) 1–7.
[2] A.K. Hamzat, A.Z. Sahin, M.I. Omisanya, L.M. Alhems, Advances in PV and PVT cooling technologies: a review, Sustain. Energy Techn. and Assess. 47 (2021) 101360.

[3] M.S. Ghoghaei, A. Mahmoudian, O. Mohammadi, M.B. Shafii, H. Jafari Mosleh, M. Zandieh, M.H. Ahmadi, A review on the applications of micro−/nano-encapsulated phase change material slurry in heat transfer and thermal storage systems, J. Therm. Anal. Calorim. 145 (2021) 245–268.
[4] C. Liu, Z. Rao, J. Zhao, Y. Huo, Y. Li, Review on nanoencapsulated phase change materials: preparation, characterization and heat transfer enhancement, Nano Energy 13 (2015) 814–826.
[5] E. Alehosseini, S.M. Jafari, Micro/nano-encapsulated phase change materials (PCMs) as emerging materials for the food industry, Trends Food Sci. Technol. 91 (2019) 116–128.
[6] K. Faraj, M. Khaled, J. Faraj, F. Hachem, C. Castelain, Phase change material thermal energy storage systems for cooling applications in buildings: a review, Renew. Sust. Energ. Rev. 119 (2020) 109579.
[7] S.L. Tariq, H.M. Ali, M.A. Akram, M.M. Janjua, M. Ahmadlouydarab, Nanoparticles enhanced phase change materials (NePCMs)-a recent review, Appl. Therm. Eng. 176 (2020) 115305.
[8] K.Y. Leong, M.R.A. Rahman, B.A. Gurunathan, Nano-enhanced phase change materials: a review of thermo-physical properties, applications and challenges, J. Energy Storage 21 (2019) 18–31.
[9] M. Ghalambaz, A. Doostani, A.J. Chamkha, M.A. Ismael, Melting of nanoparticles-enhanced phase-change materials in an enclosure: effect of hybrid nanoparticles, Int. J. Mech. Sci. 134 (2017) 85–97.
[10] N.H. Boukani, A. Dadvand, A.J. Chamkha, Melting of a Nano-enhanced phase change material (NePCM) in partially-filled horizontal elliptical capsules with different aspect ratios, Int. J. Mech. Sci. 149 (2018) 164–177.
[11] Q. Wang, L. Yang, J. Song, Preparation, thermal conductivity, and applications of nano–enhanced phase change materials (NEPCMs) in solar heat collection: a review, J. Energy Storage 63 (2023) 107047.
[12] S. Dey, B.R. Kumar, Finite element analysis of a thermal non-equilibrium hybrid nanofluid model for natural convection in a complex porous enclosure, Comput. Math. Appl. 169 (2024) 177–194.
[13] M. Zafar, H. Sakidin, M. Sheremet, I.B. Dzulkarnain, A. Hussain, R. Nazar, J. A. Khan, M. Irfan, Z. Said, F. Afzal, Recent development and future prospective of tiwari and das mathematical model in nanofluid flow for different geometries: a review, Processes 11 (3) (2023) 834.
[14] M.B. Hafeez, M. Krawczuk, A review: applications of the spectral finite element method, Arch. Comput. Meth. Eng. 30 (5) (2023) 3453–3465.
[15] H.M. Sadeghi, M. Babayan, A. Chamkha, Investigation of using multi-layer PCMs in the tubular heat exchanger with periodic heat transfer boundary condition, Int. J. Heat Mass Transf. 147 (2020) 118970.
[16] F. Selimefendigil, H.F. Oztop, A.J. Chamkha, Natural convection in a CuO–water nanofluid filled cavity under the effect of an inclined magnetic field and phase change material (PCM) attached to its vertical wall, J. Therm. Anal. Calorim. 135 (2) (2019) 1577–1594.
[17] R. Hidki, L. El Moutaouakil, M. Boukendil, Z. Charqui, Z. Zrikem, A. Abdelbaki, Natural convection heat transfer analysis of a nano-encapsulated phase change material (NEPCM) confined in a porous square chamber with two heat sources, J. Energy Storage 73 (2023) 108924.
[18] R. Hidki, L. El Moutaouakil, M. Boukendil, Z. Charqui, Z. Zrikem, A. Abdelbaki, Mixed convection and surface radiation in a ventilated cavity containing two heat-generating solid bodies, Mater. Today Proc. 66 (2022) 318–324.
[19] H. Saleh, M. Jelita, N. Md Arifin, I. Hashim, Effect of waviness on thermal-flow characteristics in an inclined trapezoidal cavity filled with nano-encapsulated phase change material and water, Numer. Heat Transf. A Appl. 84 (7) (2023) 801–818.
[20] M. Jelita, Z. Amir, H. Saleh, Free convection in two composite enclosures filled with water and nano encapsulated phase change particles, J. Energy Storage 80 (2024) 110219.
[21] A. Alhashash, H. Saleh, Convective flow analysis for moderate Rayleigh numbers of nano encapsulated phase change materials-water filled enclosure with various thermal conditions, J. Energy Storage 66 (2023) 107523.
[22] S. Basriati, H. Saleh, Mathematical modeling of unsteady convective flow analysis of water and nano-encapsulated phase change particles in composite enclosure subject to rotation, J. Energy Storage 72 (2023) 108393.
[23] C. Ho, Y.-C. Liu, M. Ghalambaz, W.-M. Yan, Forced convection heat transfer of Nano-encapsulated phase change material (NEPCM) suspension in a mini-channel heatsink, Int. J. Heat Mass Transf. 155 (2020) 119858.
[24] J. Cheng, Y. Zhou, D. Ma, S. Li, F. Zhang, Y. Guan, W. Qu, Y. Jin, D. Wang, Preparation and characterization of carbon nanotube microcapsule phase change materials for improving thermal comfort level of buildings, Constr. Build. Mater. 244 (2020) 118388.
[25] F.M. Azizul, A.I. Alsabery, I. Hashim, A.J. Chamkha, Heatline visualization of mixed convection inside double lid-driven cavity having heated wavy wall, J. Therm. Anal. Calorim. 145 (2021) 3159–3176.
[26] I. Ali, A.I. Alsabery, N. Bakar, R. Roslan, Mixed convection in a double lid-driven cavity filled with hybrid nanofluid by using finite volume method, Symmetry 12 (12) (2020) 1977.
[27] Z. Ebrahimpour, M. Sheikholeslami, S.A. Farshad, A. Shafee, Solar energy application for LFR unit with trapezoidal cavity receiver considering radiative mode, Phys. Scr. 95 (12) (2020) 125701.
[28] L. Kolsi, K. Ghachem, S. Larguech, G. AlNemer, Numerical investigation of the double diffusive convection in 3D trapezoidal solar still equipped with conductive fins, Mathematics 10 (12) (2022) 2115.
[29] N. Biswas, D.K. Mandal, N.K. Manna, A.C. Benim, Magneto-hydrothermal triple-convection in a W-shaped porous cavity containing oxytactic bacteria, Sci. Rep. 12 (1) (2022) 18053.
[30] A.M. Aly, Z. Raizah, S. El-Sapa, H.F. Oztop, N. Abu-Hamdeh, Thermal diffusion upon magnetic field convection of nano-enhanced phase change materials in a permeable wavy cavity with crescent-shaped partitions, Case Stud. Therm. Eng. 31 (2022) 101855.
[31] E. Golab, S. Goudarzi, H. Kazemi-Varnamkhasti, H. Amigh, F. Ghaemi, D. Baleanu, A. Karimipour, Investigation of the effect of adding nano-encapsulated phase change material to water in natural convection inside a rectangular cavity, J. Energy Storage 40 (2021) 102699.
[32] S.E. Ahmed, Z.A. Raizah, Analysis of the entropy due to radiative flow of nano–encapsulated phase change materials within inclined porous prismatic enclosures: finite element simulation, J. Energy Storage 40 (2021) 102719.
[33] S. Hussain, Z. Raizah, A.M. Aly, Thermal radiation impact on bioconvection flow of nano-enhanced phase change materials and oxytactic microorganisms inside a vertical wavy porous cavity, Int. Commun. Heat Mass Transf. 139 (2022) 106454.
[34] A. Alazzam, N.A. Qasem, A. Aissa, M.S. Abid, K. Guedri, O. Younis, Natural convection characteristics of nano-encapsulated phase change materials in a rectangular wavy enclosure with heating element and under an external magnetic field, J. Energy Storage 57 (2023) 106213.
[35] S. Hussain, N. Alsedias, A.M. Aly, Natural convection of a water-based suspension containing nano-encapsulated phase change material in a porous grooved cavity, J. Energy Storage 51 (2022) 104589.
[36] T. Tayebi, S. El-Sapa, N. Karimi, A.S. Dogonchi, A.J. Chamkha, A.M. Galal, Double-diffusive natural convection with Soret/Dufour effects and energy optimization of nano-encapsulated phase change material in a novel form of a wavy-walled I-shaped domain, J. Taiwan Inst. Chem. Eng. 148 (2023) 104873.
[37] M. Sadeghi, A.J. Chamkha, R. Ali, M.B.B. Hamida, M. Ghodrat, A.M. Galal, Hydrothermal behavior of micro-polar nano-encapsulated phase change materials (NEPCMs) in an inclined L-shaped cavity, Case Stud. Therm. Eng. 35 (2022) 102039.
[38] D. Huu-Quan, M. Sheremet, M.S. Kamel, M. Izadi, Investigation of thermal-hydro dynamical behavior on nano-encapsulated PCM suspension: effect of fin position, fractioning and aspect ratio, Chem. Eng. Process. Process Intensif. 157 (2020) 108122.
[39] Y. Cao, N. Farouk, H. Ayed, A.A. Aly, F. Jarad, M. Dahari, M. Wae-hayee, B. Saleh, Heat transfer improvement between a pair of heater and cooler inside an energy storage by using nano-encapsulated phase change material/water: a numerical modeling, Case Stud. Therm. Eng. 30 (2022) 101770.
[40] N.B. Khedher, H.S.S. Aljibori, S. Mehryan, A. Hajjar, M. Ghalambaz, M. Boujelbene, N.B. Elbashir, I. Mahariq, Vibrational convection in thermal systems: Nano-encapsulated phase change material in a porous enclosure, Int. Commun. Heat Mass Transf. 157 (2024) 107719.
[41] P. Reddy, P. Sreedevi, Enhanced entropy generation and heat transfer characteristics of magnetic nano-encapsulated phase change materials in latent heat thermal energy storage systems, Appl. Math. Mech. 45 (6) (2024) 1051–1070.
[42] W. Wang, Y.-H. Jin, Y.-M. Chen, Z.-M. Hu, R.-R. Zhou, H. Tian, F. Xin, X.-Z. Li, Hydrothermal and entropy generation analyses of natural convection of nano-encapsulated phase change materials suspension in a cavity subjected to the localized heating, J. Energy Storage 77 (2024) 109865.
[43] M. Kouki, M. Nayak, A.A. Pasha, A.J. Chamkha, M.K. Al Mesfer, M. Danish, K. Irshad, Thermal and irreversibility analyses of a suspension embodying nano-encapsulated phase change materials using power-law and Darcy-brinkman-Forchheimer models, case studies, Therm. Eng. 59 (2024) 104509.
[44] K. Herouz, H. Laidoudi, A. Aissa, A. Mourad, K. Guedri, M. Oreijah, O. Younis, Analysis of nano-encapsulated phase change material confined in a double lid-driven hexagonal porous chamber with an obstacle under magnetic field, J. Energy Storage 61 (2023) 106736.
[45] A.N. Sadr, M. Shekaramiz, M. Zarinfar, A. Esmaily, H. Khoshtarash, D. Toghraie, Simulation of mixed-convection of water and nano-encapsulated phase change material inside a square cavity with a rotating hot cylinder, J. Energy Storage 47 (2022) 103606.
[46] B. Bhadauria, M. Yaseen, S.K. Rawat, M. Pant, Designing machine learning based intelligent network for assessment of heat transfer performance of ternary hybrid nanofluid flow between a cone and a disk: case of MLP feed forward neural network, Comput. Math. Appl. 169 (2024) 17–38.
[47] Z. Huang, J.-C. Feng, Y. Zhuang, Coupling effects, regulation mechanisms and applications of thermal-fluid-magnetic in composite phase change systems: a comprehensive review, J. Energy Storage 118 (2025) 116200.
[48] W. Li, Y. Zhuang, J. Wang, J.-C. Feng, Evolution of vortex modes and heat transfer in metal foam/nanoparticles composite phase change materials under the combined action of centrifugal force and magnetic field, Int. J. Heat Mass Transf. 255 (2026) 127860.
[49] A.M. Galal, T. Tayebi, A.A. Pasha, V. Tirth, A. Algahtani, T. Al-Mughanam, P. Gupta, S. Qaiyum, M. Nayak, Neural modeling of nano-encapsulated PCM convection in a wavy porous enclosure with thermal radiation, Int. Commun. Heat Mass Transfer 169 (2025) 109805.
[50] T. Tayebi, A.A. Pasha, M. Danish, M.K. Al Mesfer, S. Qaiyum, M. Nayak, N.A. Shah, Artificial neural network prediction of an electrohydrodynamic thermosolutal buoyancy-driven convection of NEPCMs-dielectric suspension within an oblique enclosure with active blocks, Int. Commun. Heat Mass Transf. 169 (2025) 109756.
[51] S. Ohid, M. Nayak, R. Ali, M. Kallel, Application of an active heat transfer amelioration technique to a dielectric non-Newtonian fluid: machine learning approach, Int. Commun. Heat Mass Transf. 169 (2025) 109794.
[52] F. Alqurashi, M.A. Alomari, L.M. Ahmed, T.I. Kh, I.R. Ali, M.K. Almansoori, A. M. Hassan, O. Jabbar, Comparative machine learning analysis of double-diffusive mixed convection in a magnetohydrodynamic lid-driven curvilinear cavity containing NEPCM, Int. Commun. Heat Mass Transfer 176 (2026) 111286.

[53] M.A. Alomari, A.M. Hassan, A.M. Sadeq, F. Alqurashi, O. Jabbar, M.A. Flayyih, Thermodynamic analysis of a multi-port NEPCM cooling device: effects of mixed convection and magnetohydrodynamics on heat dissipation, Int. Commun. Heat Mass Transf. 172 (2026) 110736.
[54] S. Barlak, O.N. Sara, A. Karaipekli, S. Yapıcı, Thermal conductivity and viscosity of nanofluids having nanoencapsulated phase change material, Nanosc. Microsc. Thermophys. Eng. 20 (2) (2016) 85–96.
[55] L. Chai, R. Shaukat, L. Wang, H.S. Wang, A review on heat transfer and hydrodynamic characteristics of nano/microencapsulated phase change slurry (N/MPCS) in mini/microchannel heat sinks, Appl. Therm. Eng. 135 (2018) 334–349.
[56] B. Chen, X. Wang, R. Zeng, Y. Zhang, X. Wang, J. Niu, Y. Li, H. Di, An experimental study of convective heat transfer with microencapsulated phase change material suspension: laminar flow in a circular tube under constant heat flux, Exp. Thermal Fluid Sci. 32 (8) (2008) 1638–1646.
[57] K. Khanafer, K. Vafai, A critical synthesis of thermophysical characteristics of nanofluids, Int. J. Heat Mass Transf. 54 (19–20) (2011) 4410–4428.
[58] H.R. Seyf, Z. Zhou, H. Ma, Y. Zhang, Three dimensional numerical study of heat-transfer enhancement by nano-encapsulated phase change material slurry in microtube heat sinks with tangential impingement, Int. J. Heat Mass Transf. 56 (1–2) (2013) 561–573.
[59] A. Zaraki, M. Ghalambaz, A.J. Chamkha, M. Ghalambaz, D. De Rossi, Theoretical analysis of natural convection boundary layer heat and mass transfer of nanofluids: effects of size, shape and type of nanoparticles, type of base fluid and working temperature, Adv. Powder Technol. 26 (3) (2015) 935–946.
[60] A. Chamkha, A. Doostanidezfuli, E. Izadpanahi, M. Ghalambaz, Phase-change heat transfer of single/hybrid nanoparticles-enhanced phase-change materials over a heated horizontal cylinder confined in a square cavity, Adv. Powder Technol. 28 (2) (2017) 385–397.
[61] M. Ghalambaz, I. Pop, M. Sheremet, M.H. Ali, M. Ghalambaz, Numerical and artificial neural network analysis of magnetohydrodynamic natural convection in a nano-encapsulated phase change suspension filled quadrantal circular enclosure, J. Appl. Comput. Mech. 11 (4) (2025) 929–945.
[62] S. Hussain, A. Chattopadhyay, M.S. Aldhabani, Local thermal non-equilibrium analysis of magneto-radiative natural convection of nano-encapsulated phase change material suspension in a crown-shaped porous cavity, Int. J. Numer. Methods Heat Fluid Flow (2026) 1–33.
[63] A.A. Sakhir Abed, Numerical simulation of laminar incompressible driven cavity flow in a l-shape domain, international journal of mechanical, Eng. Technol. 10 (1) (2019) 119–132.
[64] M. Roy, S. Roy, T. Basak, Role of various moving walls on energy transfer rates via heat flow visualization during mixed convection in square cavities, Energy 82 (2015) 1–22.
[65] O.C. Zienkiewicz, R.L. Taylor, P. Nithiarasu, The Finite Element Method for Fluid Dynamics, Seventh Edition ed., Butterworth-Heinemann, Oxford, 2014.
[66] D. Pepper, The Intermediate Finite Element Method: Fluid Flow and Heat Transfer Applications, Routledge, 2017.
[67] C.T. Kelley, Solving Nonlinear Equations with Newton's Method, SIAM, 2003.
[68] P. Deuflhard, Newton Methods for Nonlinear Problems: Affine Invariance and Adaptive Algorithms, Springer Science & Business Media, 2005.
[69] M. Bollhöfer, O. Schenk, R. Janalik, S. Hamm, K. Gullapalli, State-of-the-art sparse direct solvers, in: Parallel Algorithms in Computational Science and Engineering, 2020, pp. 3–33.
[70] M. Bollhöfer, A. Eftekhari, S. Scheidegger, O. Schenk, Large-scale sparse inverse covariance matrix estimation, SIAM J. Sci. Comput. 41 (1) (2019) A380–A401.
[71] M.H. Matin, I. Pop, Natural convection flow and heat transfer in an eccentric annulus filled by copper nanofluid, Int. J. Heat Mass Transf. 61 (2013) 353–364.
[72] O. Turan, A. Sachdeva, N. Chakraborty, R.J. Poole, Laminar natural convection of power-law fluids in a square enclosure with differentially heated side walls subjected to constant temperatures, J. Non-Newtonian Fluid Mech. 166 (17) (2011) 1049–1063.
[73] M. Moallemi, K. Jang, Prandtl number effects on laminar mixed convection heat transfer in a lid-driven cavity, Int. J. Heat Mass Transf. 35 (8) (1992) 1881–1892.
[74] M. Waheed, Mixed convective heat transfer in rectangular enclosures driven by a continuously moving horizontal plate, Int. J. Heat Mass Transf. 52 (21−22) (2009) 5055–5063.
[75] R. Iwatsu, J.M. Hyun, K. Kuwahara, Mixed convection in a driven cavity with a stable vertical temperature gradient, Int. J. Heat Mass Transf. 36 (6) (1993) 1601–1608.
[76] S. Mehryan, M. Ghalambaz, L.S. Gargari, A. Hajjar, M. Sheremet, Natural convection flow of a suspension containing nano-encapsulated phase change particles in an eccentric annulus, J. Energy Storage 28 (2020) 101236.
[77] M. Ghalambaz, A.J. Chamkha, D. Wen, Natural convective flow and heat transfer of Nano-encapsulated phase change materials (NEPCMs) in a cavity, Int. J. Heat Mass Transf. 138 (2019) 738–749.